Colloids and Surfaces A: Physicochemical and Engineering Aspects 728 (2026) 138577

Contents lists available at ScienceDirect

Colloids and Surfaces A: Physicochemical and Engineering Aspects

journal homepage: www.elsevier.com/locate/colsurfa

# Field polarity effects on single and dual-droplet transport and evaporation in electric fields

Davoud Abdi Lanbaran [a,*], Pouria Farokhi Kojour [a], Chao Wang [a], Chuang Wen [b], Zhen Wu [c], Bo Li [d]

[a] School of Engineering, University of Kent, UK
[b] School of Construction Management and Engineering, University of Reading, UK
[c] Department of Process Equipment and Control Engineering, Xi'an Jiaotong University, China
[d] School of Electrical, Electronic and Mechanical Engineering, University of Bristol, UK

## HIGHLIGHTS

- A validated 2D phase-field model is used to simulate single and dual droplet dynamics under both DC and AC electric fields.
- DC fields yield up to 45 % shorter evaporation time and over twice the horizontal displacement compared to AC fields.
- Droplet coalescence occurs earlier and more consistently under DC excitation than under AC conditions.
- Field polarity, intensity, and droplet volume jointly govern displacement, coalescence, and evaporation outcomes.
- Results provide practical guidance for the design of electrohydrodynamic cooling and droplet manipulation systems.

## GRAPHICAL ABSTRACT

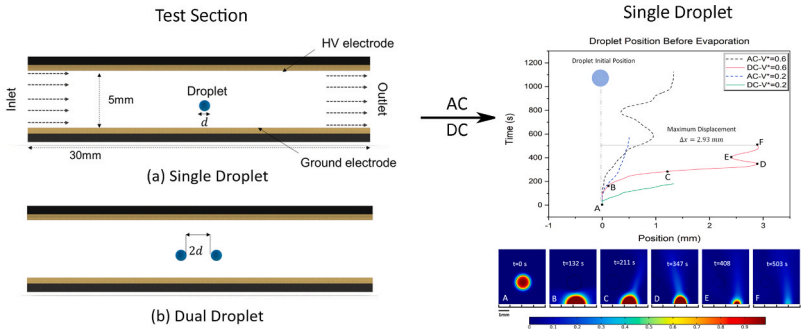


## ARTICLE INFO

*Keywords:*
Water Droplets
Electric Field
Droplet Coalescence
Evaporation

## ABSTRACT

High-voltage electric fields provide a low-energy, non-contact means of manipulating droplet dynamics, yet a systematic comparison of direct current (DC) and alternating current (AC) excitation, particularly for interacting droplet pairs, remains limited. In this study, a validated two-dimensional phase-field model in COMSOL Multiphysics is employed to simulate single and paired water droplets (normalized volume V* = 0.2–1.0) under uniform vertical fields ranging from E = 0.1–1 kV/mm. The coupled Navier–Stokes and Maxwell equations are solved to quantify droplet displacement, coalescence, and evaporation, and the model is benchmarked against experimental data with deviations below 3 %. The results show that DC excitation produces stronger displacement, faster evaporation, and earlier, more sustained coalescence, while AC requires higher field strengths and yields only intermittent merging with weaker transport effects. Importantly, the study identifies polarity-dependent thresholds: under DC fields, coalescence initiates at E_init ≈ 0.62 kV/mm and completes at E_comp = 0.77 kV/mm (V*=1), whereas under AC fields, coalescence initiates at ≈ 0.92 kV/mm and does not complete within the tested range. This systematic mapping of polarity-dependent thresholds represents the principal

* Corresponding author.
*E-mail address:* Da562@kent.ac.uk (D.A. Lanbaran).

https://doi.org/10.1016/j.colsurfa.2025.138577
Received 2 August 2025; Received in revised form 15 September 2025; Accepted 5 October 2025
Available online 7 October 2025

novelty of the work and provides a framework for interpreting electrohydrodynamic droplet behavior. The findings offer practical guidance for applications in digital microfluidics, droplet transport, and surface cooling.

## 1. Introduction

The study of water droplet behavior has attracted broad interest across numerous scientific fields due to water's distinctive physical properties, high specific heat, surface tension, and electrical conductivity, which render its dynamic behavior complex to model and predict. Researchers have explored various techniques to control droplet dynamics, including thermal excitation [1], magnetic fields [2], and surfactants [3], each yielding valuable insights. Among these methods, high-voltage electric fields have garnered particular attention due to their energy efficiency [4], precise control, and localized influence on droplet behavior [5]. When applied with well-designed electrodes and suitable voltage levels, electric fields allow for precise manipulation of droplet shape, evaporation, and motion. In particular, droplet displacement is crucial for applications such as surface cleaning and fluidic transport [6], where controllability and repeatability are essential.

Water droplets respond strongly to electric fields due to their high electrical conductivity. The alignment of field lines affects droplet polarization [7], influencing deformation, coalescence, and movement [8, 9]. These effects are central to technologies such as electrowetting [10], electrospraying [11], and electrocoalescence [12], which rely on interfacial charge dynamics to enable controlled droplet manipulation. Under electric excitation, droplets may deform from spherical shapes into ellipsoidal or flattened structures, and nearby electric fields can induce coalescence between adjacent droplets [13]. Electric-field-driven droplet motion, particularly lateral displacement, has growing relevance in targeted cooling, drug delivery, and microscale surface cleaning [14, 15]. Several key parameters influence this behavior: electric field strength, electrode configuration, and polarity type (AC or DC) [16]. Foundational work by Atten [17] established the electrohydrodynamic forces acting on droplets suspended in insulating fluids, which has since been expanded through both experimental and numerical studies. Eow and Ghadiri [18] showed that droplet motion and shape deformation stem from the competition between interfacial tension and electrical stress. Sun et al. [19] observed that applying an electric field significantly enhances droplet velocity along predefined paths. Similarly, Li et al. [20] demonstrated that stronger vertical electric fields increase droplet elongation and detachment from surfaces. Collectively, these behaviors are governed by the interaction between electrostatic, viscous, and gravitational forces [21].

Among the most influential factors affecting droplet dynamics is coalescence, which can substantially alter a droplet's size, velocity, evaporation time, and mobility [22]. As shown by Mugele et al. [23], coalescence does not occur automatically upon contact; it depends on a complex interplay of electrohydrodynamic forces, interfacial energy, and spacing. The initial gap between droplets has proven to be critical. Studies by Liu et al. [26] and others [24,25] reveal that spacing equivalent to one to two droplet diameters enables strong interactions while preserving coalescence control. This spacing regime is often captured through the non-dimensional ratio $S_0/R_0$, which is directly linked to the electric Bond number and merging thresholds. Here, $R_o$ denotes the initial radius of the reference droplet ($V^* = 1$), and $S_o$ denotes its corresponding surface area. These quantities are used as scaling parameters throughout the study: $R_o$ provides the characteristic length scale for displacement normalization, while $S_o$ serves as the baseline surface area for evaporation comparisons [27]. Furthermore, the type of electric field has a profound influence on coalescence behavior. DC fields generate steady Maxwell stress, promoting sustained attraction and earlier merging [28]. In contrast, AC fields induce periodic polarity changes that disturb interfacial stability, delaying or even preventing coalescence [29]. These polarity-dependent differences are crucial for designing electrohydrodynamic systems used in digital microfluidics, surface cleaning, and electrically enhanced heat transfer devices [30, 31].

In addition to altering droplet shape and motion, electric fields also affect evaporation rates. Water droplets become polarized and migrate toward regions of higher potential, driven by interactions between the applied field and the induced dipole. The strength of this effect depends on field intensity and electrical conductivity, both of which also influence thermal transfer and evaporation [32]. Chen et al. [33] reported that DC fields elongate droplets along the field axis and accelerate evaporation below 0.7 kV/mm. Li et al. [34] demonstrated complete evaporation of large droplets under strong DC fields up to 3.67 kV/cm. Moreover, steady DC fields generate sustained ionic wind and net momentum flux, often an order of magnitude higher than equivalently rated AC fields due to polarity reversal in AC that cancels flow over time [35]. Liu et al. [36] developed models incorporating gravity, surface tension, and electric forces to predict evaporation under vertical fields, while Al-Mohammadi and Fazli [37] directly linked evaporation time to field strength.

Despite substantial progress, important knowledge gaps persist. Specifically, the field strength thresholds that define the transitions between droplet coalescence, horizontal displacement, and evaporation have not been systematically characterized, particularly in the context of AC versus DC excitation. To ensure reliability, the model is validated against experimental benchmarks, including evaporation time and displacement data from Li et al. [46], Chen et al. [47], and Huang et al. [48], as detailed in Section 3.1. To address this, we present a comprehensive numerical study of water droplet behavior under uniform vertical DC and AC electric fields. A validated two-dimensional phase-field model is used to simulate both single-droplet and dual-droplet configurations across a range of droplet volumes and field intensities. Particular attention is given to how coalescence affects horizontal displacement and evaporation time under each type of electric field. To our knowledge, this is the first systematic numerical comparison of AC and DC field effects on both single and interacting droplets. The results provide a unified understanding of how electric field polarity, strength, and droplet volume govern interfacial dynamics. These insights offer practical guidance for optimizing electrohydrodynamic droplet control in applications such as microfluidic routing, surface cooling, and droplet-based cleaning technologies.

## 2. Methodology

### 2.1. Numerical model and geometry

A two-dimensional numerical model was developed to simulate the behavior of both single and adjacent water droplets suspended in air. The simulations were conducted using the Finite Element Method (FEM) within the COMSOL Multiphysics environment. This model focused on assessing the influence of a vertically applied electric field on droplet displacement, coalescence, and evaporation, with the electric field interactions captured through the incorporation of Maxwell stress tensor components. The primary objective was to evaluate how exposure to alternating (AC) and direct current (DC) electric fields alters the overall behavior of water droplets. The computational domain was designed as a simple flat rectangular channel, including inlet and outlet boundaries for air circulation, as illustrated in Fig. 1. In cases involving electric fields, the top wall of the channel was defined as the high-voltage electrode, while the bottom wall served as the ground electrode, thereby establishing a vertical field across the droplets. For AC field

cases, a sinusoidal voltage of 60 Hz was applied to the top electrode, expressed as $v(t) = v_0 \sin(2\pi ft)$, where $v_0$ is the amplitude and f= 60 Hz. This frequency was selected to ensure several oscillation cycles during the droplet's lifetime, allowing meaningful observation of quasi-static AC field effects. If the frequency is high enough, the cycle-averaged electric field is considered to dominate the net force on the droplets.

### 2.2. Modelling

A phase-field approach was employed to simulate the motion and interaction of water droplets under the influence of an electric field [38]. This method is particularly suitable for modelling two-phase flows with moving interfaces, as it allows for smooth transitions in density and other physical properties across phase boundaries [39]. It effectively captures phase changes or the coexistence of materials with distinct characteristics within a single-phase domain [40,41]. In this model, the phase-field variable ($\varnothing$) transitions continuously between $-1$ and $+1$ across the interface region, representing the change between fluid phases. The thickness of the interface is controlled by a parameter ($\epsilon$), which determines the gradient of this transition. The evolution of the phase field and its coupling to fluid motion is governed by the Cahn–Hilliard equations [42]:

$$\frac{\partial \varnothing}{\partial t} + \mathbf{u} \bullet \nabla \varnothing = \nabla \bullet \frac{3\gamma\sigma\epsilon}{2\sqrt{2}} \nabla\varphi \tag{1}$$

$$\varphi = -\nabla \bullet \epsilon^2 \nabla \varnothing + (\varnothing^2 - 1)\varnothing \tag{2}$$

Here, $\gamma$ represents the mobility coefficient, $\sigma$ is the surface tension, and $\epsilon$ is the interface thickness control parameter. In COMSOL Multiphysics, the mobility coefficient $\gamma$ is defined as:

$$\gamma = \frac{4\sqrt{2}}{3} \frac{u_{max}}{\sigma} \tag{3}$$

where $u_{max}$ is the maximum velocity magnitude in the domain. These equations govern how the interface evolves and interacts with the surrounding fluid. Material properties such as density $\rho$, viscosity $\mu$, and permittivity $\varepsilon$ are assumed that to vary smoothly across the interface. This variation is modeled using the following generic interpolation equation:

$$\alpha = \alpha_1 + 0 \bullet 5(\alpha_2 - \alpha_1)(\varnothing + 1) \tag{4}$$

where $\alpha$ can be any of the aforementioned properties. As shown in Eq. (4), the expression simplifies at the extremes of the phase field:

$$\varnothing = 1 \rightarrow \alpha = \alpha_2 \tag{5}$$

$$\varnothing = -1 \rightarrow \alpha = \alpha_1 \tag{6}$$

Using these formulations, all physical fields such as density, velocity, and pressure are calculated as continuous functions across the interface, ensuring a stable numerical solution even in the presence of dynamic droplet interactions.

### 2.3. Governing equations

To simulate two-phase laminar flow, the governing equations are based on the incompressible Navier–Stokes formulation. The momentum and continuity equations for fluid motion are expressed as follows [43]:

$$\rho\left(\frac{\partial \mathbf{u}}{\partial t} + \mathbf{u} \bullet \nabla \mathbf{u}\right) = -\nabla p + \mu \nabla^2 \mathbf{u} + \mathbf{F}_{st} + \rho g + \mathbf{F}_{ef} \tag{7}$$

$$\nabla \bullet \mathbf{u} = 0 \tag{8}$$

Here, $\rho$ is the fluid density, $\mu$ is the dynamic viscosity, u is the velocity vector, p is the pressure field, g represents gravitational acceleration, $\mathbf{F}_{st}$ denotes the surface tension force, and $\mathbf{F}_{ef}$ is the volumetric electric field force. Surface tension is dominant for the liquid phase and is modeled as [44]:

$$\mathbf{F}_{st} = \sigma k \mathbf{n} \tag{9}$$

$$\mathbf{n} = \nabla \varnothing \tag{10}$$

where $\sigma$ is the surface tension coefficient, k is the curvature of the interface defined as $1/R$ (with units of $1/m$), and n is the normal vector to the interface, approximated by the gradient of the phase field variable $\varnothing$. The electric field force $\mathbf{F}_{ef}$ is introduced as a volumetric body force due to the interaction between the electric field and the fluid, and is defined using the divergence of the Maxwell stress tensor T [45]:

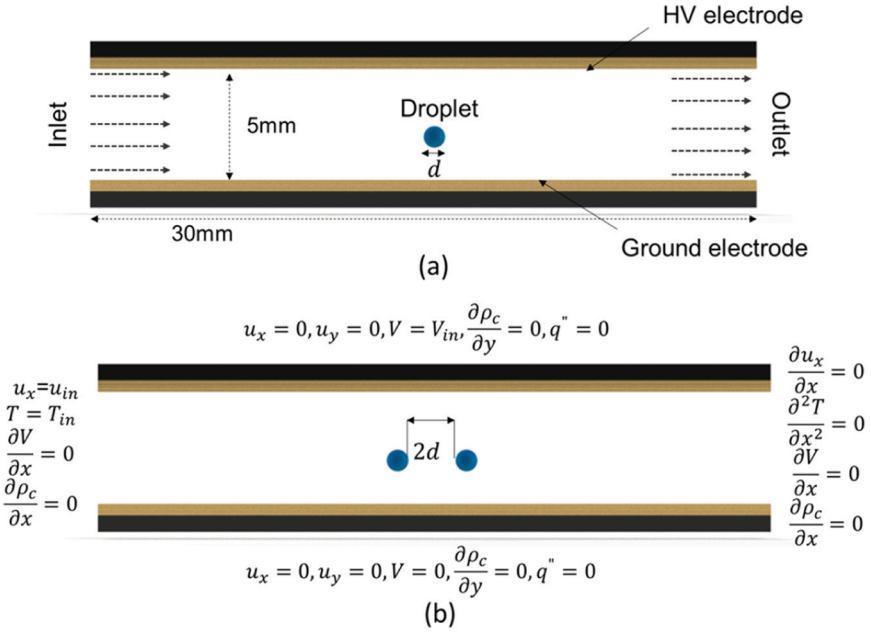


**Fig. 1.** Geometry and boundary conditions in the test section.

$$\mathbf{F_{ef}} = \nabla \bullet \mathbf{T} = qE - \frac{1}{2}E^2\nabla\varepsilon + \frac{1}{2}\nabla\left(E^2\frac{d\varepsilon}{d\rho_m}\rho_m\right) \quad (11)$$

In this equation, E is the electric field vector, q is the free charge density, and $\rho_m$ is the material density. The three terms on the right-hand side represent:

- The electrophoretic (Coulomb) force, which acts on free charges and is proportional to both the electric field and charge density,
- The dielectrophoretic force, which arises from permittivity gradients across the interface between two fluids with different dielectric properties, and
- The electrostriction force, which results from spatial gradients in electric field magnitude and compressibility of the medium.

These electric field-induced forces are key in capturing the droplet deformation, movement, and coalescence behavior under AC and DC fields. Although the bulk air phase is assumed to be quasi-charge free, localized interfacial charges accumulate at the droplet boundary due to polarization, making the Coulomb term (qE) relevant at the interface while negligible in the surrounding air.

### 2.4. Boundary conditions

The computational domain and boundary conditions for the simulations are illustrated in Fig. 1, which includes two configurations: a single-droplet setup (Fig. 1a) and a dual-droplet setup (Fig. 1b). In both cases, the domain consists of a rectangular channel, with airflow entering from the left inlet (assigned a constant velocity profile) and exiting through the right outlet (defined by a fixed pressure condition to maintain stable mass flow). Electrically, the top wall of the domain serves as the high-voltage electrode, where either a direct (DC) or alternating (AC) electric potential is applied. The bottom wall acts as the ground electrode at zero potential, establishing a vertical electric field across the droplet(s). All solid walls are treated as no-slip boundaries for fluid flow and are electrically insulated, except for the electrodes. These conditions are applied consistently across all cases to allow for direct comparison between AC and DC field effects. The droplets are initialized with their centers positioned 1 mm above the ground electrode, corresponding to a radius $R_0$= 1 mm, such that the lower interface is already in direct contact with the surface at t = 0. In this setup, the droplets are assumed to be pre-spread and pinned, and dynamic wetting or spreading processes are not explicitly modeled. This setup was chosen to replicate realistic impact dynamics and capture interfacial behavior during the contact event. At initialization, the droplet was at rest, undeformed, and assigned a spherical shape corresponding to its prescribed volume. The phase-field variable (∅) was defined such that ∅ = 1 within the droplet and ∅ = 0 in the surrounding air. This initial condition enabled accurate simulation of droplet–wall interactions, including deformation and spreading upon impact. Fig. 1a shows a centrally placed single droplet, used to track horizontal displacement under the influence of the electric field. Fig. 1b presents the dual-droplet configuration, with two adjacent droplets placed side by side at a center-to-center spacing approximately twice the droplet diameter, based on prior electrohydrodynamic studies [27]. This spacing allows strong electric field coupling and the potential for coalescence, while avoiding premature merging at the outset. For clarity, two thresholds are distinguished in this study: coalescence initiation (E_init), defined as the first reproducible appearance of a liquid bridge connecting the droplets that persists for multiple time steps, and coalescence completion (E_comp), defined as the voltage at which merging becomes irreversible, producing a single droplet that subsequently evolves as a unified body. To ensure size-independent comparison, the non-dimensional droplet volume V*is introduced as:

$$V^* = \frac{V}{V_0} \quad (12)$$

where V is the volume of the droplet and $V_0$ is the volume of the largest droplet, corresponding to a diameter of 1 mm. All other droplet volumes were scaled accordingly to allow consistent evaluation of displacement, coalescence, and evaporation behaviors under various electric field conditions. The applied electric field was varied between E = 0.1 and 1.0 kV/mm, consistent with values reported in experimental electrohydrodynamic droplet studies [46,47]. This range avoids negligible forcing at very low fields (<0.1 kV/mm) and prevents unphysical dielectric breakdown at very high fields (>1 kV/mm). The normalized droplet volume range (V* = 0.2–1.0) corresponds to diameters of 0.2–1.0 mm, representative of droplets in microfluidic transport and cooling applications, while also ensuring stable numerical resolution for capturing size-dependent effects.

These boundary conditions and geometric setups are essential for isolating the effects of electric field type and intensity on droplet behavior. By comparing single- and dual-droplet dynamics, the study quantitatively assesses how coalescence influences both evaporation rate and lateral displacement under electric excitation.

### 2.5. Numerical workflow

The overall computational procedure implemented in this study is outlined in the flowchart presented in Fig. 2. The simulation begins with the definition of initial physical properties and field variables, including fluid density, surface tension coefficient, electric permittivity, and the initial phase-field distribution (∅).

The core of the simulation couples the Navier–Stokes momentum equations (Eq. 7) with body forces arising from both surface tension and electric field interactions. Upon initialization, the phase-field variable (∅) is used to determine the water volume fraction and the interface location within the computational domain. This, in turn, allows for the evaluation of surface tension forces (Eq. 9) and electric field forces (Eq. 11), both of which depend on local phase and material properties. With the interfacial forces computed, the momentum and continuity equations (Eqs. 7,8) are solved simultaneously to obtain the updated velocity and pressure fields. The solution process continues iteratively, with the solver updating the phase field, recomputing the body forces, and solving the governing equations until convergence is achieved. The simulation is considered converged when the residuals of all governing equations fall below a predefined threshold set within the COMSOL solver. This iterative approach ensures consistent coupling between hydrodynamic behavior, electric field interaction, and droplet interface evolution, allowing for an accurate prediction of droplet displacement, deformation, and coalescence over time.

### 2.6. Assumptions

The numerical simulation of the two-phase droplet system is based on the following assumptions to simplify the physical model and reduce computational complexity:

- The variation in airflow velocity and temperature along the channel is assumed to be negligible, resulting in a quasi-uniform external environment.
- Standard temperature and pressure (STP) conditions are applied to both the surrounding air and the water droplet throughout the simulation.
- The concentration of free electric charges in the bulk air is considered negligible, so the gas phase can be treated as quasi-electrostatic and charge-free. However, interfacial polarization at the droplet–air boundary generates localized charges, which are represented in the Coulomb force term of Eq. (11).
- Internal moisture distribution and temperature gradients within the droplet are assumed to be negligible, enabling a uniform droplet composition and temperature.

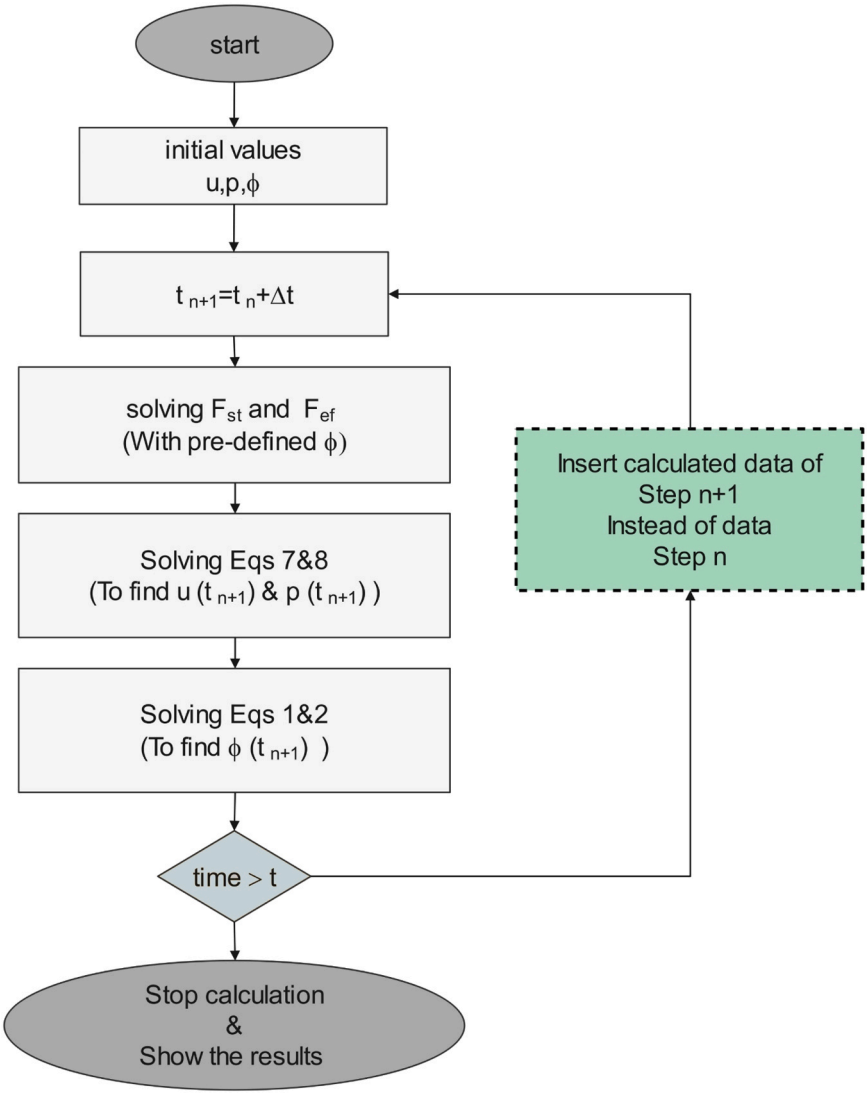


**Fig. 2.** Flowchart of the numerical simulation.

- A no-slip condition is imposed at all solid-fluid interfaces to account for boundary layer behavior near the walls and droplet surface.
- The model also assumes an idealized configuration: surfaces are perfectly smooth (no roughness), internal droplet temperature gradients are neglected, and capillary fluctuations are not resolved. By simplifying surface and temperature conditions, the model isolates the main electrohydrodynamic mechanisms, but it may slightly overpredict mobility or underrepresent thermocapillary variations.
- The model is formulated in two dimensions, which captures the essential deformation, coalescence, and evaporation dynamics but does not represent three-dimensional instabilities, axisymmetric variations, or exact surface-area scaling.

These assumptions ensure that the model remains computationally efficient while accurately capturing the dominant physics governing droplet deformation, motion, and coalescence under electric fields.

### 2.7. Grid independence

Mesh independence is a critical aspect of finite element simulations, ensuring that numerical results remain consistent regardless of further mesh refinement. In this study, five mesh densities were evaluated under both AC and DC electric field cases to determine an optimal configuration that balances computational cost and solution accuracy. The results of this analysis are presented in Fig. 3, which shows the computed velocity magnitude (left vertical axis) and water volume fraction (right vertical axis) at a reference point located at the center of the domain ($x = 15$ mm, $y = 2.5$ mm). The velocity magnitude was calculated using the combined horizontal and vertical velocity components.

As the number of mesh elements increased from 4460 to 92154, both velocity and volume fraction values exhibited strong convergence. Specifically:

- The velocity magnitude decreased from $9.14 \times 10^{-2}$ m/s (4460 elements) to $8.33 \times 10^{-2}$ m/s (92154 elements), with the difference between the fourth (31613 elements) and fifth mesh (92154 elements) being less than 0.5 %.
- The water volume fraction increased from $1.90 \times 10^{-2}$ to $2.80 \times 10^{-2}$, with a negligible difference ($<0.02 \times 10^{-2}$) between the final two mesh levels.

These results confirm that the fourth mesh configuration, with 31,613 elements, achieves mesh-independent accuracy while significantly reducing computational time compared to finer meshes. Thus, this mesh was used for all subsequent simulations.

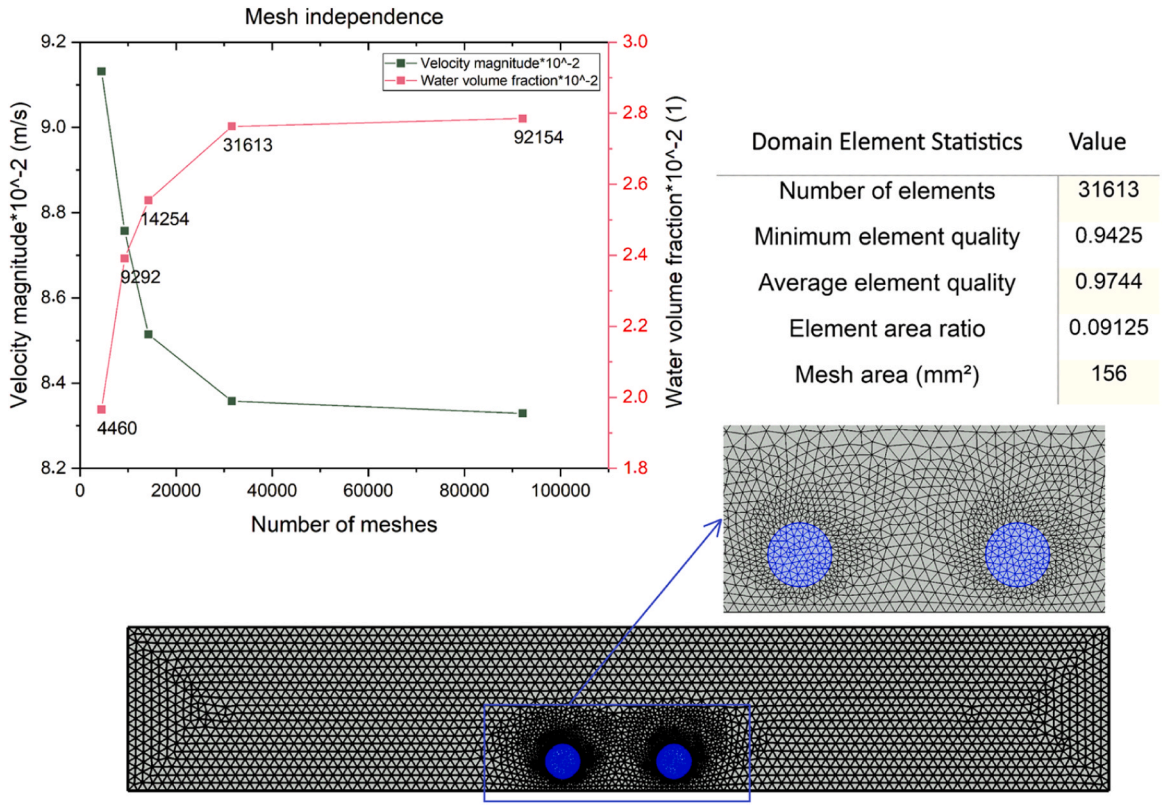


**Fig. 3.** Evaluation of mesh independence with five mesh configurations.

## 3. Results and discussion

### 3.1. Research validation

To validate the accuracy of the developed numerical model, two key physical phenomena were compared against experimental data from the literature: (a) droplet evaporation time under applied electric fields, and (b) droplet displacement along a surface in DC conditions. Fig. 4a presents the evaporation time of a surface droplet as a function of applied electric field strength for both AC and DC configurations. The results of this study are compared with the experimental data of Li et al. [46] and Chen et al. [47]. In all cases, increasing the electric field intensity leads to a noticeable reduction in evaporation time, driven by enhanced internal circulation and surface dynamics. The DC field shows a steeper decrease compared to AC, confirming its stronger influence on droplet evaporation. The numerical predictions closely align with the reference data, with deviations remaining below 3 %, confirming the model's ability to capture the coupled thermal and electrohydrodynamic behavior.

Fig. 4b illustrates the total displacement of a droplet subjected to a DC electric field, compared against the experimental data reported by Huang et al. [48]. The displacement increases with field strength up to 0.5–0.6 kV/mm and then declines due to increased resistance and contact line pinning at higher voltages. The peak displacement observed in

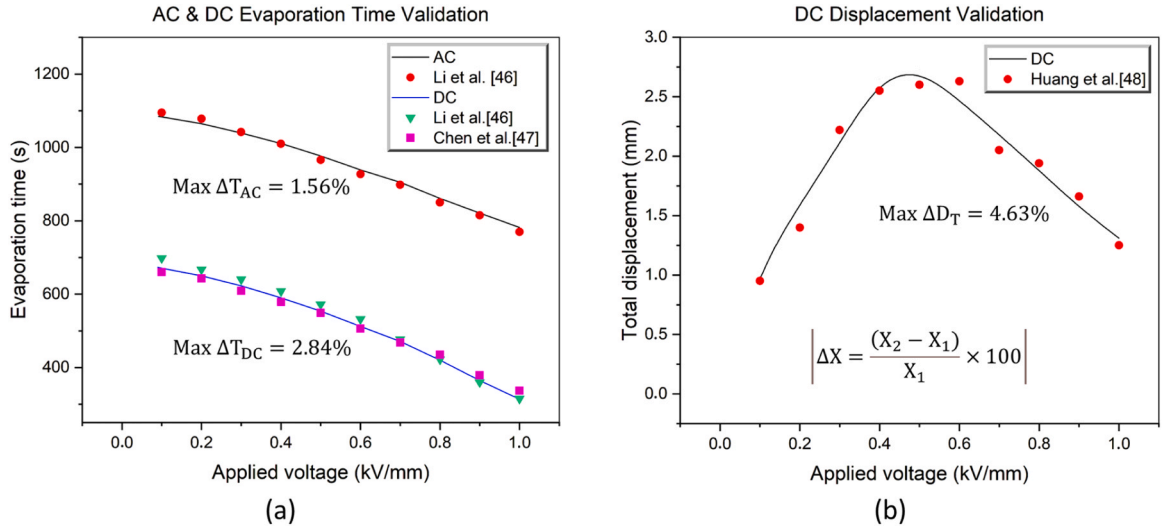


**Fig. 4.** Model validation: (a) based on evaporation time under AC and DC electric fields; (b) based on total droplet displacement under DC electric field.

this study is 2.73 mm, closely matching Huang et al.'s [48] 2.63 mm, with maximum differences below 0.09 mm. This agreement confirms that the model effectively captures surface tension forces, electrostatic pressure, and droplet–substrate interactions. Together, these validation results confirm that the numerical framework accurately replicates key droplet behaviors under electric fields. The agreement with experimental benchmarks across both thermal and displacement metrics demonstrates the reliability and physical consistency of the proposed model for simulating electrically actuated droplet dynamics. It is important to emphasize that these validation results correspond to isolated droplets. In such single-droplet cases, DC excitation enhances deformation, increases effective interfacial area, and accelerates evaporation relative to AC fields. In contrast, in dual-droplet systems discussed later (Section 4.2), DC-driven coalescence alters the surface-area-to-volume ratio in a way that delays evaporation despite ongoing deformation. This distinction underscores the need to treat single- and dual-droplet regimes separately when interpreting the influence of field polarity on evaporation.

### 3.2. Droplet deformation and evaporation process under electric field

Fig. 5 illustrates the evaporation process of a water droplet under a DC electric field with a non-dimensional volume of $V^* = 0.4$ and an applied voltage of 0.6 kV/mm. At initialization, the droplet is prescribed in a pre-spread state, represented as a disc-like form consistent with the static contact angle, reflecting the balance of gravitational and adhesive forces rather than a dynamic spreading process. Once the electric field is applied, electrostatic forces dominate the droplet dynamics. Owing to its higher permittivity relative to air, the droplet becomes polarized, generating Maxwell stresses that act unevenly across its interface. After the initial flattening caused by gravity and adhesion (disc-like state at $t = 3.7$ s), the applied field polarizes the droplet and generates Maxwell stresses that elongate the droplet vertically. Consequently, the apparent contact angle increases, and evaporation accelerates due to the enhanced interfacial deformation.

At approximately $t = 147$ s, fine halo-like droplets begin detaching from the main droplet and accelerate toward the high-voltage electrode. This marks the onset of interface instability, enhancing surface area and promoting mass transfer. The droplet continues to evaporate until it fully disappears at $t = 491$ s. After this point, microdroplets are observed migrating through the electrode channel under the influence of electric field gradients and airflow. Some of these may become ionized and be carried away with the bulk flow. These observations confirm that the electric field significantly enhances the evaporation rate, not only by deforming the droplet but also by inducing internal circulation, electrohydrodynamic effects, and interface destabilization. This qualitative behavior forms the basis for the quantitative evaporation time analysis presented in Fig. 6. In this study, evaporation time is defined as the duration between the initial application of the electric field and the complete disappearance of the droplet. This metric is especially important in applications such as EHD dryers, inkjet printing, and microfluidic cooling systems, where precise control of evaporation dynamics is essential. As shown in Fig. 6, evaporation time decreases consistently with increasing electric field intensity in both AC and DC modes. However, a clear distinction emerges: droplets subjected to DC electric fields evaporate significantly faster than those in AC fields, particularly at moderate to high voltages. For example, at a field strength of 1 kV/mm, a droplet with a non-dimensional volume of $V^* = 1$ evaporates in approximately 1104 s under DC conditions, compared to 1997 seconds in an AC field.

This difference arises from the fundamental nature of the electric field. In DC fields, the applied force is unidirectional and continuous, causing sustained deformation of the droplet interface. This promotes elongation, thinning, and eventual detachment of surface elements, all of which enhance mass transfer and accelerate evaporation. In contrast, AC fields alternate rapidly in direction and polarity, producing a symmetric distribution of field lines. The net force on the droplet interface is averaged out over time, resulting in weaker deformation and less effective internal circulation, which delays evaporation. Additionally, the rate of evaporation improvement with increasing voltage is steeper in DC fields. This is quantified by the slope angle $\theta$, which is 17.35° for DC and only 8.69° for AC, confirming the stronger response of droplets to DC excitation. The superior effectiveness of DC fields is further emphasized for larger droplets, where gravitational and adhesive forces

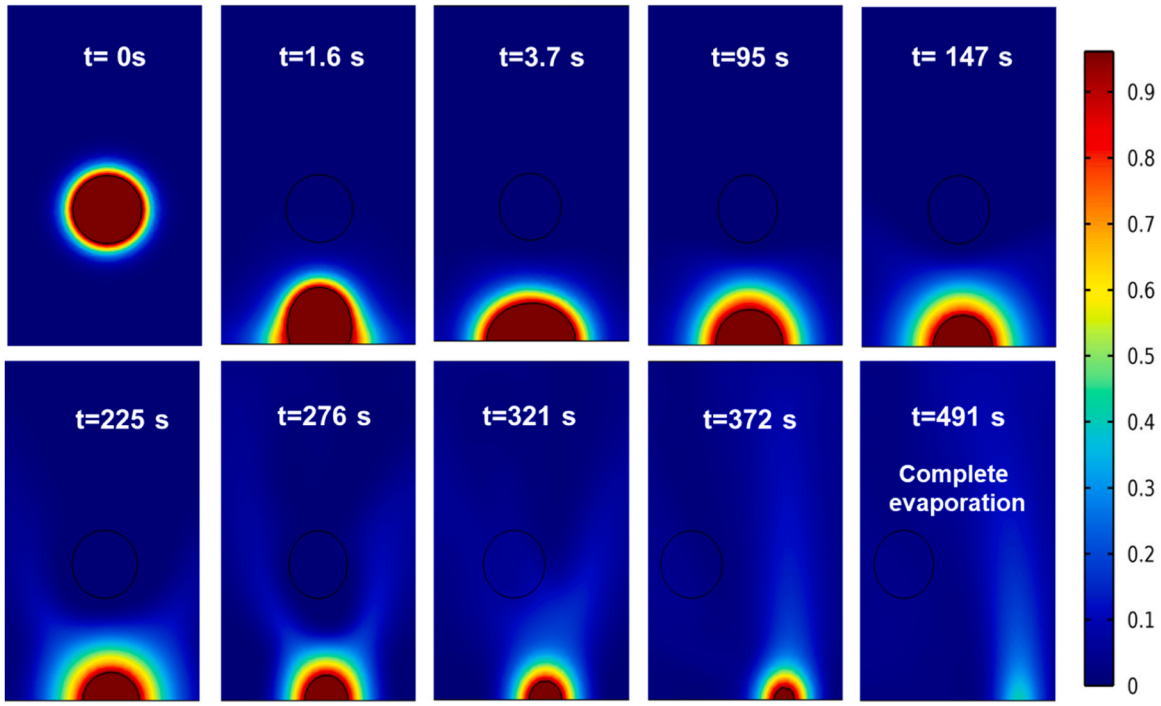


**Fig. 5.** Transformations in a droplet during evaporation ($V^* = 0.4$, $E = 0.6$ kV/mm).

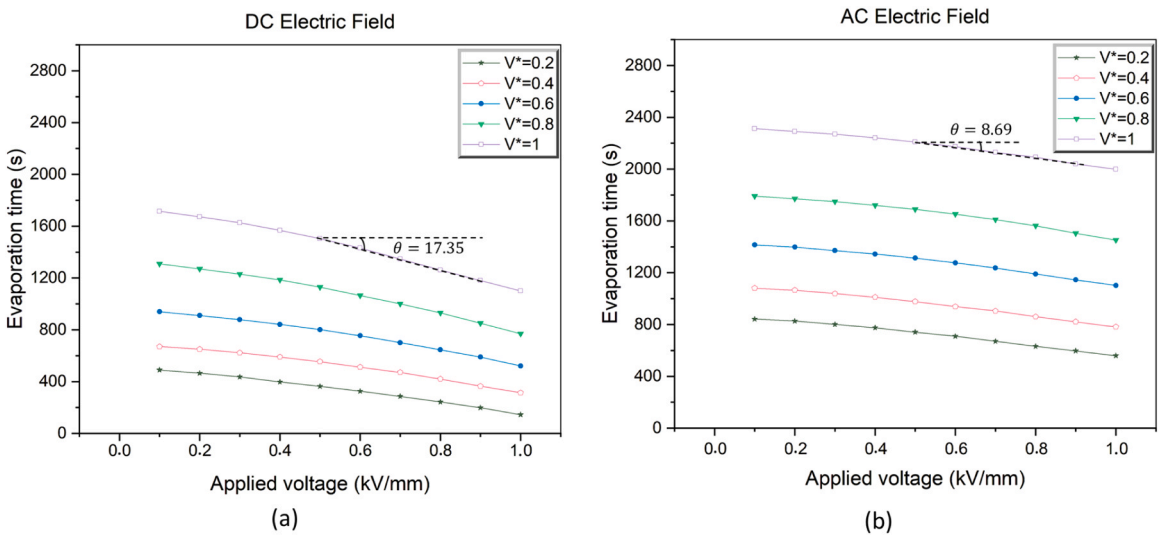


**Fig. 6.** The evaporation time of a single droplet under the effect of (a) DC electric field, (b) AC electric field.

are more dominant. These forces require greater electric stress to be overcome, something DC fields achieve more efficiently due to their focused, continuous action. In summary, the results in Fig. 6 confirm that DC electric fields are significantly more effective than AC fields at enhancing evaporation dynamics, especially for droplets with larger volumes or under stronger field intensities. It is important to note that this evaporation enhancement mechanism applies specifically to isolated droplets, where sustained deformation increases effective interfacial area and accelerates mass transfer. In dual-droplet systems, however, DC-driven coalescence alters the surface-area-to-volume ratio, which can prolong evaporation despite ongoing deformation. These contrasting behaviors emphasize the need to distinguish between single-droplet (deformation-dominated) and dual-droplet (coalescence-dominated) regimes when interpreting evaporation trends.

### 3.3. *Droplet horizontal displacement*

The use of electric fields to control droplet motion on solid surfaces has attracted growing attention in applications such as surface cleaning, microfluidic transport, and enhanced wetting. In this study, the imposed electric field induces notable horizontal displacement of the droplet, with its trajectory strongly influenced by both the type and strength of

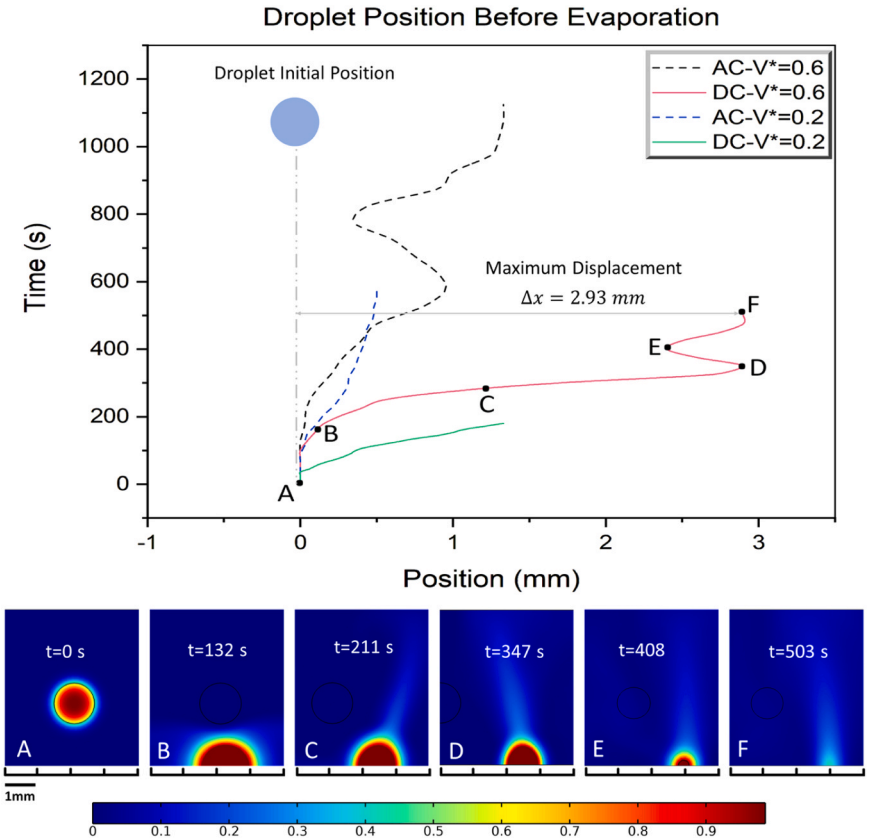


**Fig. 7.** Horizontal displacement of the droplet under AC and DC electric fields for V* = 0.2 and V* = 0.6.

the field. Fig. 7 presents the time–position behavior of a droplet subjected to DC and AC electric fields at two non-dimensional voltage levels (V*=0.2 and V*=0.6), along with contour snapshots (A–F) highlighting the droplet evolution under DC, V*= 0.6 conditions. At t = 0 s (Point A), the droplet is stationary, with a symmetric vapor concentration field. For all cases, a stabilization period of approximately 200 s follows, during which electric double layers form and electrokinetic forces begin to build. Around t = 132 s (Point B), early signs of polarization and vapor accumulation emerge, and by t = 211 s (Point C), the droplet initiates forward motion toward the electrode under the combined effects of electrostriction and electroosmotic forces.

In the DC field, the motion becomes progressively stronger. From Point C to Point D (t = 347 s), the droplet advances steadily, eventually reaching a maximum horizontal displacement of Δx = 2.93 mm at t = 503 s (Point F). While the overall motion appears smooth and unidirectional, a subtle zigzag behavior is observed between Points D and E, reflecting a temporary stick–slip mechanism at the contact line. This stick–slip behavior was not imposed through explicit surface roughness but emerges naturally from the phase-field/contact-angle formulation. In this framework, small oscillations of the order parameter at the contact line create localized pinning–depinning dynamics, which act as a numerical analogue of surface energy barriers on an idealized smooth substrate. As Marangoni stresses accumulate, the droplet overcomes the pinning, slips forward, and slightly recoils due to capillary restoring forces before resuming its forward motion. This localized fluctuation illustrates the role of interfacial dynamics even under steady forcing. The sustained motion in DC is driven primarily by the constant force component, which promotes vapor asymmetry and continuous thermocapillary flow. The contour snapshots show increasing droplet deformation and stretching during motion, with shear intensification near the contact line and the formation of jet-like features. In contrast, under the AC electric field, the droplet exhibits a reciprocating trajectory. The oscillating polarity produces alternating electroosmotic flows, causing back-and-forth motion. Although some net displacement may occur, its magnitude is much smaller than in the DC case, particularly at V*= 0.6. The alternating motion reduces net transport but increases the effective surface contact, potentially enhancing particle removal efficiency. At lower voltages (V*=0.2), both AC and DC cases show reduced displacement, but the DC field still results in greater net motion. This highlights the critical role of electric field strength in droplet manipulation. The stark contrast between AC and DC trajectories underscores the importance of field continuity in achieving directional transport. Finally, while the electric field provides the primary driving force, the overall displacement behavior also depends on interface deformation, local vapor gradients, and variations in electrostriction forces. These coupled effects collectively determine the droplet's path and its effectiveness in dynamic surface interactions.

### 3.4. Droplet total movement

Fig. 8 presents the total horizontal displacement of droplets as a function of applied voltage (E = 0–1.0 kV/mm) for various non-dimensional volumes (V*=0.2–1.0) under both DC and AC electric fields. The results highlight a strong dependence on field type, strength, and droplet size, with clear trends emerging for each case. Under DC excitation (Fig. 8a), droplet displacement follows a nonlinear and non-monotonic trend. At lower voltages (E = 0.1–0.3 kV/mm), displacement is minimal, especially for smaller droplets. As voltage increases, displacement rises sharply and peaks around 0.6–0.7 kV/mm. This peak is most pronounced at V* = 1.0, with a maximum displacement of approximately 7.2 mm. Beyond this optimal range, displacement decreases, likely due to accelerated evaporation, contact line pinning, or interfacial instability, which hinder continued motion. These behaviors demonstrate the efficiency of DC fields for droplet transport, attributed to their unidirectional Maxwell stress. However, they also reveal the importance of voltage optimization, as excessively strong fields can reduce performance.

In contrast, displacement under AC fields (Fig. 8b) increases more gradually and monotonically with both voltage and droplet size. At V* = 1.0, for instance, displacement grows steadily from under 1 mm at 0.1 kV/mm to about 3.3 mm at 1.0 kV/mm. No peak or saturation is observed in this range, indicating a continuous but less efficient propulsion mechanism. This behavior stems from the oscillatory nature of AC fields, where polarity reversals introduce opposing forces that partially cancel net motion. Consequently, AC-driven displacement is limited compared to DC excitation. Overall, DC fields consistently outperform AC fields in achieving long-range droplet transport, often more than doubling the displacement achieved at equivalent voltages. Regardless of field type, increasing V* enhances displacement due to greater electrostatic force, stronger surface-driven flows, and prolonged evaporation time. Larger droplets also promote flow stability and resist rapid mass loss, allowing them to travel further before vaporization dominates. To further clarify the influence of droplet size on transport, the total lateral displacement was normalized by the initial droplet diameter ($\Delta x/D_o$). Fig. 9 presents the normalized displacement for droplets with V*= 0.2–1.0 under DC (Fig. 9a) and AC (Fig. 9b)

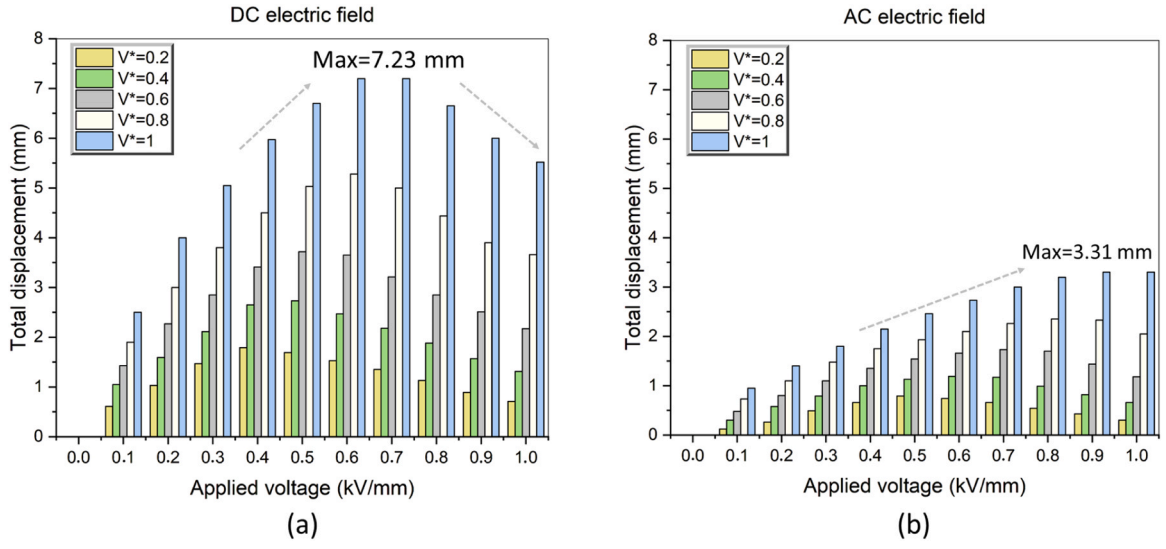


**Fig. 8.** Total horizontal displacement of droplets under AC and DC electric fields at various V* values.

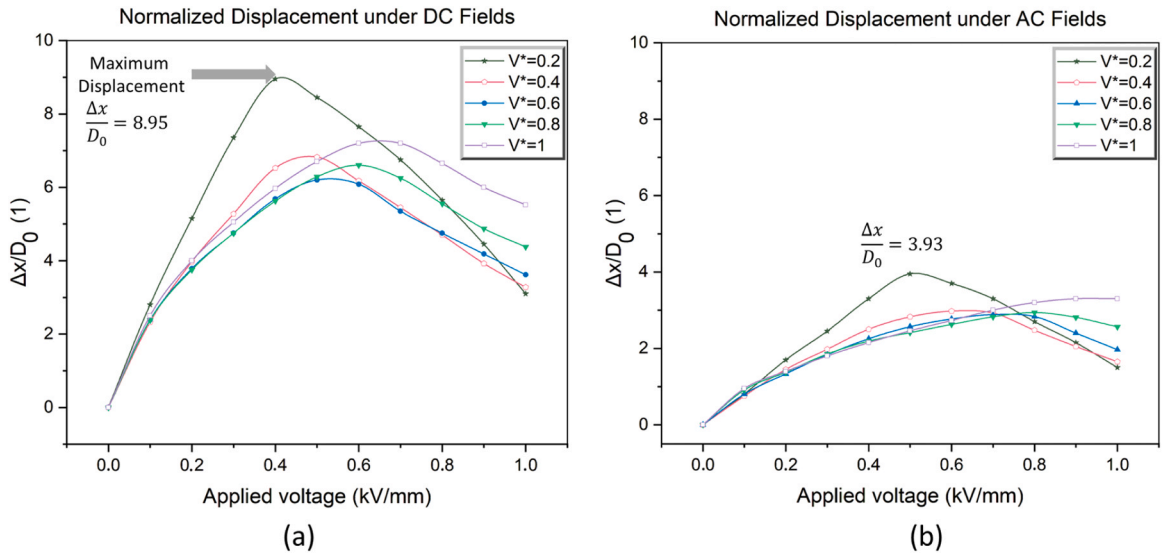


**Fig. 9.** Normalized displacement ($\Delta x/D_o$) of droplets with different volumes (V*= 0.2–1.0) under (a) DC and (b) AC electric fields.

excitation.

Under DC fields (Fig. 9a), normalized displacement increases sharply with applied voltage, reaching maxima between 0.4 and 0.6 kV/mm. The strongest response occurs for the smallest droplet (V*= 0.2), which attains $\Delta x/D_o \approx 8.95$ at E = 0.4 kV/mm. Larger droplets show progressively lower peaks: 6.83 (V*= 0.4, 0.5 kV/mm), 6.20 (V* = 0.6, 0.5 kV/mm), 6.60 (V* = 0.8, 0.6 kV/mm), and 7.20 (V*= 1.0, 0.6–0.7 kV/mm). At higher voltages, displacement declines in all cases (e.g., V*= 0.2 drops to 3.1 at 1.0 kV/mm) due to stronger resistive forces and contact-line pinning. This confirms that DC excitation produces strong size-dependent scaling: smaller droplets travel disproportionately further relative to their size, whereas larger droplets retain higher absolute displacement but lower normalized values. This behavior arises because smaller droplets have a higher surface-to-volume ratio, making them more responsive to electrostatic stresses relative to their mass, whereas larger droplets experience stronger gravitational and viscous resistance that limits normalized displacement. In contrast, AC excitation (Fig. 9b) yields much weaker displacement and minimal size dependence. Peak normalized values are significantly lower, $\Delta x/D_o = 3.93$ for V* = 0.2 (0.5 kV/mm), ≈ 2.85 for V* = 0.6,0.8 (0.5–0.6 kV/mm), and 3.3 for V*= 1.0 (1.0 kV/mm). Unlike DC fields, where displacement decreases strongly after the peak, AC responses plateau or decline only gradually, as periodic polarity reversal suppresses net motion and reduces sensitivity to droplet size. Collectively, these results highlight a fundamental distinction: DC fields amplify size effects, producing disproportionately high normalized displacement in smaller droplets, while AC fields suppress size dependence, yielding more uniform but weaker transport. This demonstrates that DC forcing is more effective for long-range droplet motion, whereas AC excitation may be advantageous for controlled, limited displacement.

## 4. Dual-droplet interaction under electric fields

While single-droplet behavior provides important baseline insights, studying two-droplet interactions offers a more realistic understanding of droplet dynamics in practical applications such as digital microfluidics, EHD cooling, and lab-on-chip systems. The presence of a second droplet introduces new physical phenomena, most notably coalescence, which alters the system's interfacial area, evaporation rate, and flow characteristics. Under the influence of electric fields, droplets not only deform but also interact through changes in vapor distribution and induced airflow. These effects are strongly dependent on the type and intensity of the electric field. In particular, DC fields tend to accelerate merging and enhance directional motion, while AC fields create oscillatory behavior that may delay coalescence and alter flow symmetry. This section investigates how two adjacent droplets interact under AC and DC fields, beginning with an analysis of how electric field conditions affect the airflow and velocity field around the droplets.

### 4.1. Velocity field and flow pattern analysis between two droplets

Within this physically relevant parameter range (E = 0.1–1.0 kV/mm; V* = 0.2–1.0), clear polarity-dependent differences emerge in terms of displacement magnitude and trajectory stability. Fig. 10 presents a comparative analysis of the velocity fields and flow profiles around two adjacent droplets (V*=0.6) under DC electric fields of 0.4 kV/mm and 0.8 kV/mm. The figure includes both velocity magnitude contours and vertical centerline velocity profiles, capturing the evolution of airflow behavior and its interaction with droplet dynamics over time. At the lower voltage of 0.4 kV/mm, the flow remains largely laminar and symmetric, with only minor disturbances near the droplets. Velocity contours show that the incoming shear flow bypasses the droplets smoothly, generating localized recirculation zones downstream of each droplet. These weak vortices are confined and remain independent throughout the simulation. Corresponding velocity profiles across the vertical centerline exhibit near-symmetry, with slight deviations (within ±0.02 m/s) emerging over time. By t = 750 s, the profile stabilizes, indicating a quasi-steady regime. No signs of droplet interaction or coalescence are observed, confirming isolated and predictable dynamics at this voltage level.

In contrast, the simulation at 0.8 kV/mm reveals a marked transition in flow behavior. Stronger Maxwell stresses give rise to high-velocity jets and counter-rotating vortices, particularly in the space between droplets. These vortices become progressively more unsteady and interconnected, leading to significant airflow deformation and enhanced momentum exchange. Velocity profiles exhibit rapid evolution from an initially symmetric state to complex multi-peak patterns. By t = 50 s, flow velocities reach + 0.06 m/s and 0.04 m/s, with persistent oscillations continuing up to t = 1500 s, indicating the absence of a steady regime. This pronounced flow instability correlates with droplet coalescence, which reshapes the local flow domain and induces strong fluid-structure interactions. The merged droplet geometry alters shear distributions, amplifies local turbulence, and accelerates droplet transport. These results emphasize that electric field strength not only governs droplet motion but also significantly modifies the surrounding flow environment. In summary, increasing the applied DC electric field from

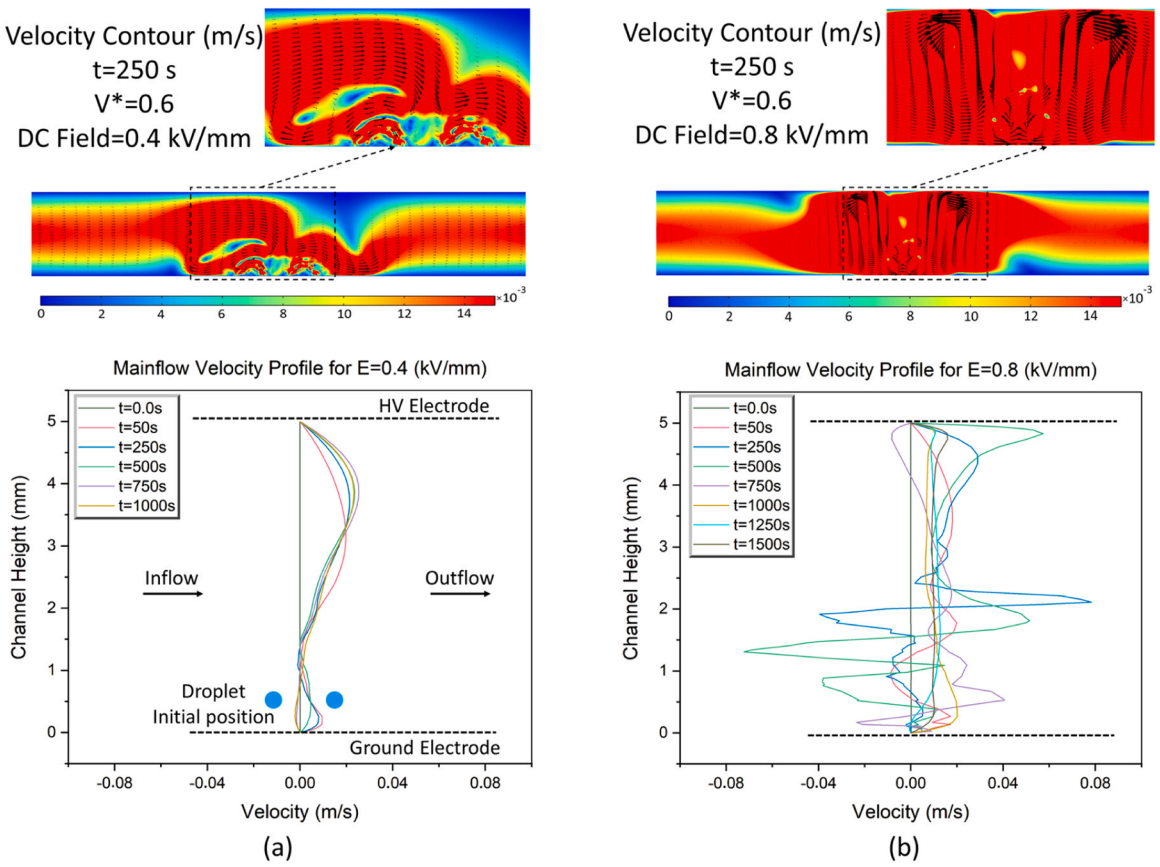


**Fig. 10.** Velocity contours and mainflow profiles around dual droplets (V* = 0.6) under DC electric fields at E = 0.4 and 0.8 kV/mm.

0.4 kV/mm to 0.8 kV/mm transitions the system from laminar, non-interacting flow to a regime characterized by vortex generation, unstable velocity profiles, and coalescence-driven disturbances. These flow transformations directly impact droplet displacement and evaporation, highlighting the critical role of electric field intensity in electrohydrodynamic manipulation. Fig. 11 illustrates the droplet coalescence process under a DC electric field with an applied intensity of E = 1 kV/mm, for droplets with a dimensionless volume of V*= 1. Coalescence refers to the merging of two adjacent droplets into a single larger droplet when brought into proximity by external forces, such as electric or magnetic fields. Once their interfacial membranes make contact, capillary and interfacial forces drive the fusion process, resulting in the collapse of the individual interfaces into a unified structure.

The frame sequence in Fig. 11 captures this phenomenon in detail. Initially, the droplets move toward one another due to electrostatic attraction. By t = 221 s, convergence becomes evident, and full coalescence is observed around t = 302 s. At a finer time resolution, the onset of merging can be detected at Δt = 0.0553 s, where the contact region shows early deformation. Notably, no sharp velocity gradient is visible at this stage, suggesting that the initial coalescence is dominated by surface tension and interfacial energy minimization, rather than by momentum transfer. By Δt = 1.07 s, the droplets have fully fused, completing the integration into a single, larger droplet. Beyond geometrical transformation, droplet coalescence significantly influences the velocity field, evaporation characteristics, and dynamic response under the electric field. Compared to individual droplets, the coalesced droplet exhibits a lower surface-area-to-volume ratio, which reduces the available interfacial area for evaporation. Consequently, the rate at which water vapor is extracted and accelerated toward the high-voltage electrode decreases. This leads to slower mass loss and an extended evaporation duration. Additionally, the larger merged droplet possesses greater structural flexibility, enabling more pronounced deformation and lateral displacement under DC excitation. This response is enhanced by the unidirectional and continuous nature of DC electric fields, which maintain a stronger net driving force overtime compared to AC fields. As a result, the coalesced droplet demonstrates improved stability, residence time, and electrohydrodynamic response, making it a key mechanism for controlling droplet behavior in electrically enhanced evaporation systems.

### *4.2. Evaporation time and coalescence behavior of dual droplets under electric fields*

Fig. 12 presents the total evaporation time of two adjacent droplets with varying dimensionless volumes (V*=0.2–1.0) under both DC and AC electric fields. This analysis aims to elucidate how droplet coalescence affects evaporation dynamics in contrast to single-droplet behavior. As the applied electric field intensifies, particularly under moderate to high strengths, electrohydrodynamic interactions between neighboring droplets become more pronounced, often resulting in coalescence. When droplets merge, the resulting geometry exhibits a reduced surface-area-to-volume ratio, which directly impacts heat and mass transfer, thereby slowing the evaporation process. Here we distinguish coalescence initiation (E_init), the first reproducible appearance of a liquid bridge (neck formation) that persists for multiple time steps, from coalescence completion (E_comp), defined as irreversible fusion into a single droplet with subsequent single-body evolution.

Fig. 12a shows that under DC fields, the evaporation time initially decreases monotonically with increasing voltage. For example, the evaporation time for a droplet with V* = 1.0 begins at approximately 1800 s in the absence of an electric field and decreases steadily until E = 0.5 kV/mm. To isolate the influence of coalescence, a linear reference trend line is constructed based on this pre-coalescence behavior. Beyond E = 0.55 kV/mm, deviations from this reference emerge,

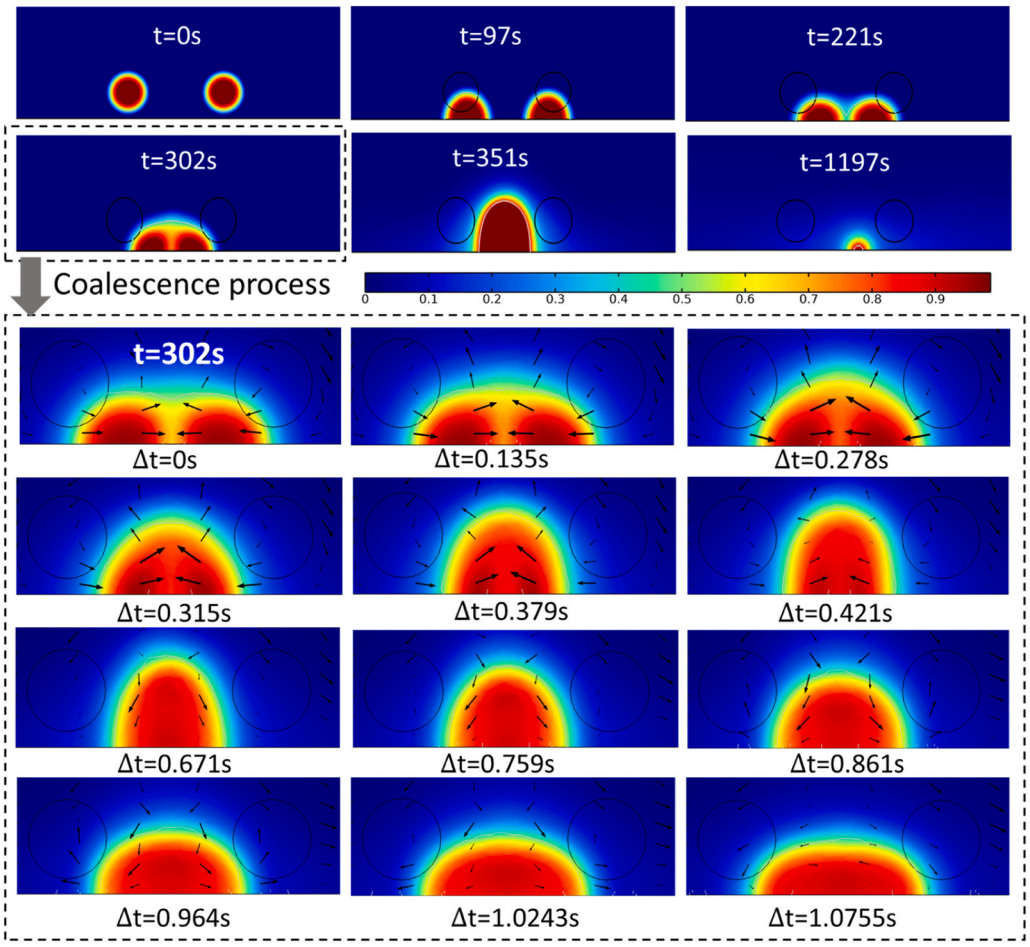


**Fig. 11.** Coalescence process under the influence of E = 1 kV/mm electric field for V*= 1.

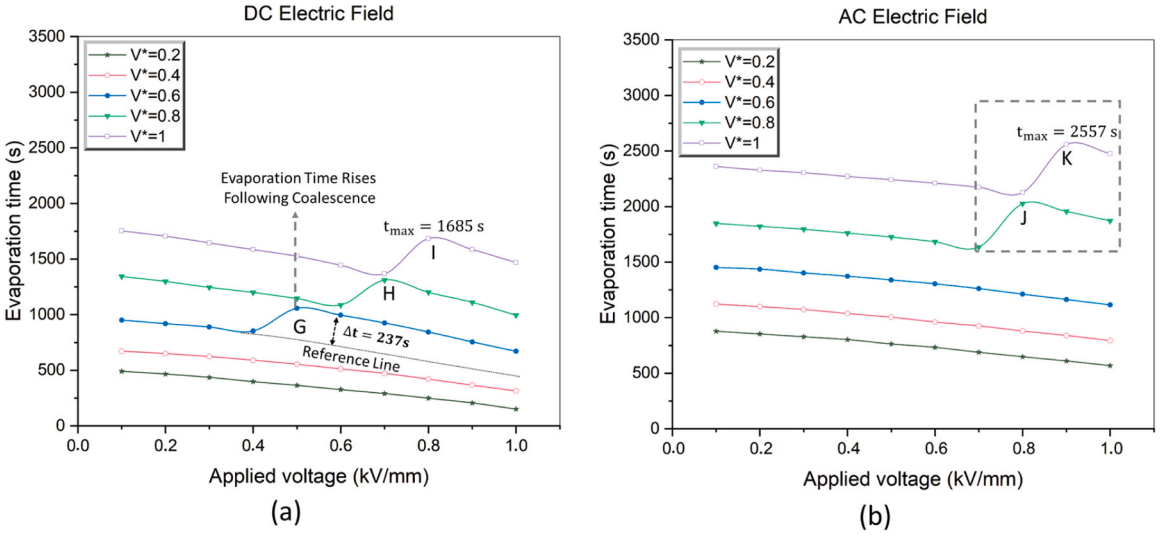


**Fig. 12.** Evaporation time for dual droplets under AC and DC electric fields.

indicating the onset of coalescence effects, particularly for V* = 0.6 and 0.8, which begin to diverge upward. For instance, the evaporation time for V* = 0.6 increases from the expected 813 s on the reference line to about 1050 s, a delay of Δt = 237 s caused by droplet merging. This reflects the altered heat transfer conditions resulting from the lower interfacial area of the combined droplet. This mechanism contrasts fundamentally with the single-droplet regime (Section 3.1), where deformation increases interfacial area and accelerates evaporation. In dual-droplet systems, however, coalescence reduces the effective surface-area-to-volume ratio, slowing evaporation despite ongoing deformation. Thus, DC fields can both enhance evaporation in isolated droplets and delay it once coalescence dominates. We note that the

upward deviation at 0.62 kV/mm marks the coalescence initiation threshold (E_init: first persistent liquid bridge), while sustained and irreversible merging is achieved at the completion threshold (E_comp = 0.77 kV/mm for V* = 1), where the droplets merge into a single body. The abstract values (0.77 kV/mm for DC and 0.92 kV/mm for AC), therefore, correspond to completion or sustained events, whereas Fig. 12 highlights the earlier initiation of DC-driven coalescence. Similar behavior is observed at points H and I for V* = 0.8 and 1.0, with a global maximum evaporation time of approximately 1685 s at V* = 1.0. At higher voltages, the curves resume their downward trend, as intensified electrostatic stress overcomes the stabilizing effect of coalescence. In contrast, Fig. 12b illustrates the response under AC electric fields. The evaporation time declines more gradually and consistently across all V* values. For V* = 1.0, the initial evaporation time is around 2400 s, and it slowly decreases with increasing voltage. Although coalescence does occur, its impact is significantly weaker and appears only at higher field strengths. Subtle local maxima, such as point J for V* = 0.8 (near 2030 s) and point K for V* = 1.0 (2557 s), indicate mild prolongation due to coalescence. However, these effects are far less pronounced than in the DC case. The alternating polarity of AC fields disrupts the sustained interface deformation and contact required for stable coalescence, thereby limiting its influence on evaporation duration. It is noted that changes in evaporation time are expected to scale with droplet surface area; however, since the present study employs a two-dimensional framework, this proportionality can only be qualitatively inferred. A full three-dimensional model would be required for quantitative confirmation. Overall, these results highlight the crucial role of electric field type and magnitude in determining droplet evaporation and coalescence behavior. DC electric fields, with their unidirectional Maxwell stress, promote persistent droplet merging at intermediate voltages, delaying evaporation due to the geometric transformation. In contrast, AC fields suppress long-lasting coalescence due to polarity reversal, which continuously alters the force direction and weakens interfacial bonding. This distinction is especially evident within the 0.62–0.77 kV/mm range, where DC-induced coalescence most strongly amplifies the evaporation time. Such behavior must be carefully accounted for in applications requiring precise control of evaporation dynamics, thermal transport, or droplet manipulation efficiency.

### 4.3. Force analysis and total horizontal displacement of dual droplets

To better understand the underlying mechanisms governing droplet displacement under electric field excitation, Fig. 13a presents the time evolution of the vertical component of the body force (N/m$^3$) and the corresponding velocity vectors at six distinct time intervals (t = 0–1500 s). These results reveal how electrohydrodynamic interactions shape droplet motion from the initial stationary state to eventual coalescence and downstream transport.

At t = 0 s, both droplets remain static, and the force field displays a symmetric distribution with negligible vertical components (on the order of $10^{-4}$ N/m$^3$, indicating minimal motion. Upon applying the electric field, significant changes arise: by t = 100 s, strong upward body forces emerge at the apex of each droplet, reaching values exceeding 200 N/m$^3$. Simultaneously, recirculating velocity vectors form in the wake regions behind the droplets, initiating lateral displacement toward one another. Between t = 200 s and t = 300 s, the droplets converge and merge into a single larger structure. This coalescence event intensifies the vertical force, which peaks around 467 N/m$^3$, and generates more prominent wake vortices. The resulting merged droplet induces major reconfiguration of the surrounding flow field, characterized by stronger shear layers and asymmetrical recirculation patterns. From t = 900 s to 1500 s, the coalesced droplet continues to move downstream under the sustained influence of the electric field and airflow. During this phase, while the forward vertical body force at the droplet's leading edge gradually diminishes, a strong suction effect develops in the rear wake region. This suction zone is marked by negative

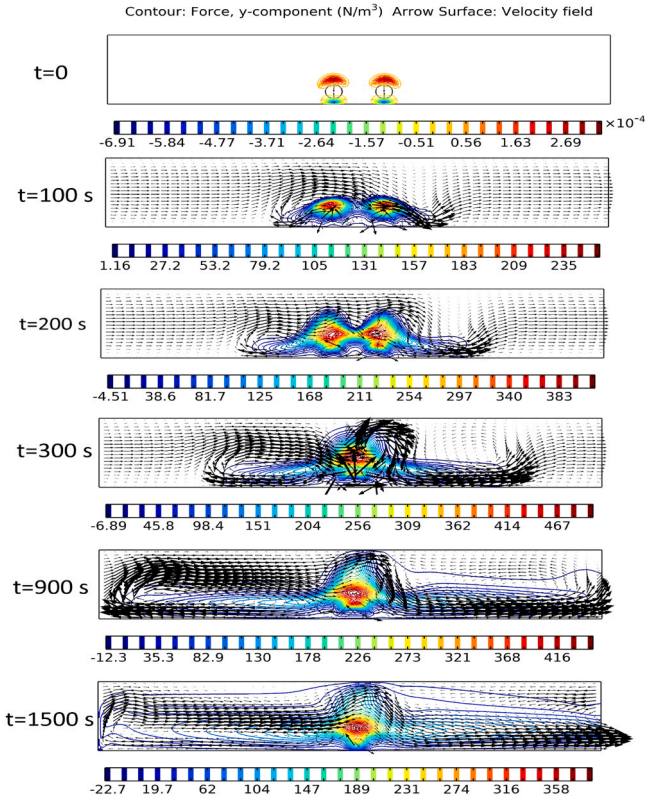


**Fig. 13.** Force Contours and Velocity Arrows under Electric Field for V*= 1 and E = 1 kV/mm.

vertical force values, reaching a minimum of approximately –22.7 N/m$^3$. The velocity vector field reveals the formation of an elongated, low-pressure channel extending behind the droplet, which effectively guides it downstream toward the outlet. These results suggest that long-range droplet displacement under DC electric fields is governed by two coupled mechanisms: (1) the upward body force concentrated at the droplet front, which drives initial motion, and (2) the rear wake suction, which sustains displacement by reducing pressure resistance. Together, these effects facilitate efficient transport of the merged droplet through the domain, with the coalescence event serving as a critical transition point in the overall motion trajectory. To further elucidate the mechanisms governing droplet displacement and coalescence under electric field excitation, Fig. 14 presents the time evolution of vorticity magnitude and the vertical component of the volume force for both single and dual-droplet configurations under DC and AC electric fields. This comparison highlights critical dynamical differences in how field type and droplet interaction influence interfacial force generation and flow behavior.

Under DC electric field excitation (left panel), the vertical volume force rises rapidly after field initiation, particularly in the dual-droplet case, which peaks at approximately 2283 N/m$^3$ around t = 274 s. This peak coincides with the onset of droplet coalescence, marked by the gray vertical bar. The vorticity magnitude also increases in parallel, reaching a maximum of 28.5 s$^{-1}$ shortly after coalescence. Compared to the single-droplet configuration, the dual-droplet case exhibits consistently higher force and vorticity, indicating that droplet interaction amplifies both electric body forces and rotational flow dynamics. The DC field maintains stable and sustained force and vorticity levels after the peak, reflecting continuous wake development and steady propulsion. In contrast, the AC electric field (right panel) exhibits a more transient response. The dual-droplet configuration again demonstrates an early force peak (2120 N/m$^3$) near t = 280 s, followed by a sharper decline compared to the DC case. Interestingly, the maximum vorticity under AC

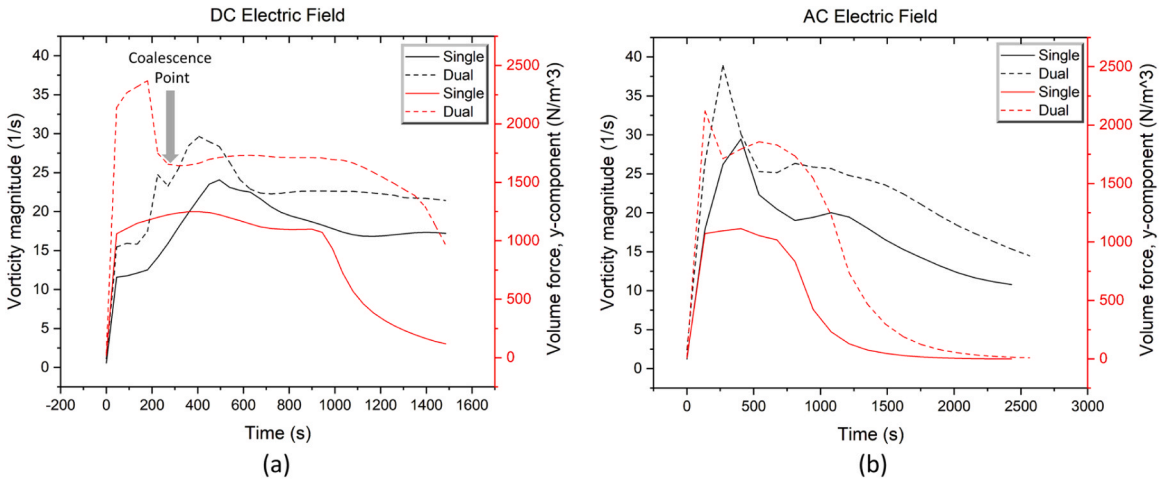


**Fig. 14.** Volume Force and Vorticity Trends in Single vs. Dual Droplet Configurations.

excitation slightly exceeds that under DC, reaching about 38 $s^{-1}$ . While this may initially seem counterintuitive due to the oscillatory nature of AC fields, it is consistent with theoretical expectations. The time-varying Maxwell stress in AC excitation causes rapid accelerations and reversals in shear direction, which promote abrupt local deformation and short-lived eddy formation. These effects amplify instantaneous vorticity during the early stages, despite lacking a sustained net driving force. This distinction explains why higher peak vorticity under AC does not translate into greater displacement: the alternating polarity causes successive vortices to oppose one another, cancelling net transport. In contrast, DC excitation maintains a lower but continuous vorticity that builds cumulatively, driving stronger wake structures and yielding significantly greater long-range displacement. Beyond t = 500 s, both the vertical force and vorticity decay more quickly under AC excitation. This decline reflects the weaker net propulsion in AC fields due to the periodic cancellation of opposing forces. Although the dual-droplet configuration maintains higher values than the single-droplet case throughout the simulation, the differences gradually diminish as the system approaches a low-activity regime with reduced droplet motion and interface stress. Overall, the results in Fig. 14 reinforce the conclusion that DC electric fields are more effective for sustained droplet transport. The unidirectional nature of the DC field supports stronger and longer-lasting volume forces and wake-induced vorticity. While AC fields can generate transiently stronger shear and localized rotational structures, their alternating polarity limits cumulative displacement and long-term stability. Moreover, the comparison between single and dual-droplet cases highlights the amplifying role of droplet interaction, particularly in the pre-coalescence phase, where interface proximity enhances both force generation and flow rotation. Understanding the displacement behavior of droplets on surfaces is critical for applications such as microfluidic actuation, particle transport, and surface cleaning. In this study, the lateral motion of two adjacent droplets is examined under both DC and AC electric field excitation, with the results illustrated in Fig. 15. Displacement trajectories are plotted against electric field strength for various normalized droplet volumes (V* = 0.2–1.0).

The results demonstrate that DC electric fields induce significantly greater droplet displacement than AC fields, primarily due to the continuous and unidirectional nature of Maxwell stresses under DC excitation. This persistent body force enables more effective droplet propulsion. For all droplet sizes, displacement initially increases with electric field intensity, reaches a peak, and then declines at higher voltages, highlighting the competing effects of electric force, coalescence, and evaporation. For instance, larger droplets (V* → 1) under DC reach a maximum displacement of 17.52 mm at E = 0.82 kV/mm (Point L), whereas AC excitation yields a maximum of around 7.6 mm at E = 0.92 kV/mm (Point M), less than half the DC-induced displacement.

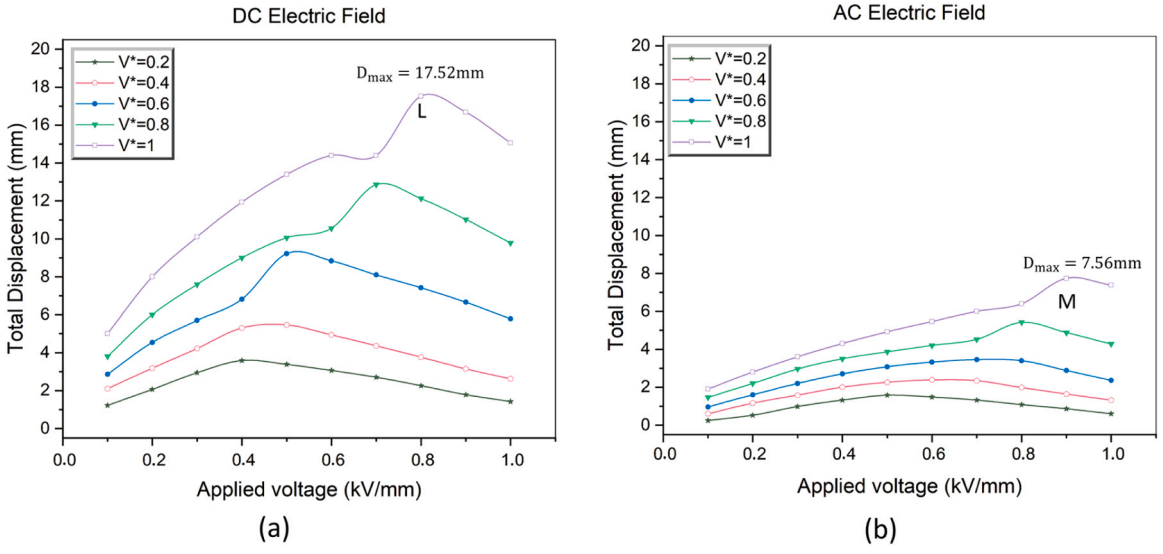


**Fig. 15.** Total displacement for dual droplets under AC and DC electric fields.

This trend of DC superiority persists across all droplet volumes, though smaller droplets achieve lower peak displacements and reach their maxima at lower voltages. The decline in displacement beyond the peak is attributed to accelerated evaporation and droplet instability, which reduce the effective driving force. In contrast, AC fields induce more gradual, monotonic displacement growth with no clear peak observed in the tested range. This is due to the alternating polarity of AC excitation, which periodically offsets the forward motion, resulting in lower net transport. Additionally, larger droplets consistently exhibit greater displacement than smaller ones, benefiting from enhanced momentum and stability. Optimal displacement for small droplets typically occurs at moderate voltages (0.4–0.6 kV/mm), where the field is strong enough to initiate motion without inducing premature evaporation. Overall, DC fields prove substantially more effective for long-range droplet transport, offering over twice the displacement capacity of AC fields at equivalent voltages. These findings underscore the critical role of field polarity and droplet size in electrohydrodynamic control, providing actionable insights for designing microfluidic systems that rely on precise droplet actuation, such as surface cleaning, bioassay delivery, and lab-on-a-chip platforms.

### 4.4. Polarity-dependent thresholds and regimes of droplet behavior

Fig. 16(a–c) and Table 1 present a detailed analysis of how the driving voltage polarity, specifically the relative contribution of DC versus AC components, governs threshold electric fields and subsequent droplet behavior. The waveform is parameterized by a dimensionless factor V*, where larger values indicate a stronger unipolar (DC-dominated) drive and smaller values correspond to a more alternating (AC-dominated) input. As polarity reversals increase, the droplet pair exhibits distinctly different outcomes, ranging from efficient coalescence under steady DC to complete suppression of coalescence under purely alternating fields.

To characterize these transitions, four threshold field levels are defined in Fig. 16:

- E_disp (Displacement Threshold): minimum field required for droplets to overcome surface tension and visibly displace.
- E_init (Initiation Threshold): field at which a liquid bridge first forms, marking the onset of coalescence.
- E_comp (Completion Threshold): field necessary for full merging into a single droplet.

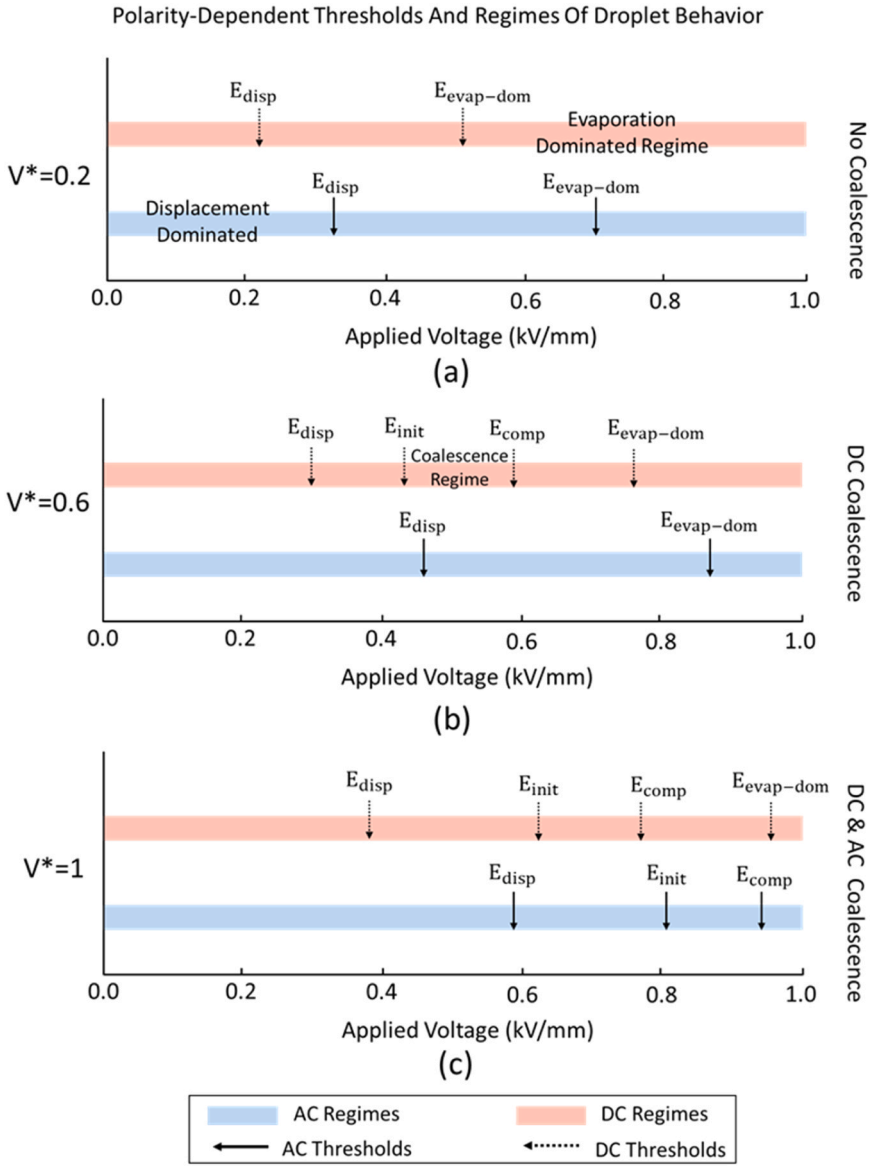


**Fig. 16.** Threshold field strengths for displacement, coalescence, and evaporation under DC (red) and AC (blue) excitation: (a) V*= 0.2, (b) V*= 0.6, (c) V*= 1.0.

**Table 1**
Threshold field values for displacement, coalescence, and evaporation at different droplet sizes.

| Droplet Size (V*) | $E_{disp}$ (DC) | $E_{disp}$ (AC) | $E_{init}$ (DC) | $E_{init}$ (AC) | $E_{comp}$ (DC) | $E_{comp}$ (AC) | Evaporation Effect $E_{evap-dom}$ |
|---|---|---|---|---|---|---|---|
| 0.2 | 0.25 | 0.35 | Not observed | Not observed | Not observed | Not observed | Evaporation accelerated (fastest, shortest lifetime) |
| 0.4 | 0.27 | 0.39 | Not observed | Not observed | Not observed | Not observed | Moderate acceleration; no delay |
| 0.6 | 0.30 | 0.45 | 0.43 | Not observed | 0.56 | Not observed | Strongest delay: + 237 s due to merging |
| 0.8 | 0.34 | 0.52 | 0.55 | 0.73 | 0.64 | 0.85 | Slight delay at ~0.6–0.7 (kV/mm) |
| 1.0 | 0.39 | 0.59 | 0.62 | 0.82 | 0.77 | 0.92 | Delay at 0.8 kV/mm, larger than other droplet sizes |

- E_evap-dom (Evaporation-Dominated Threshold): field beyond which evaporation or atomization dominates, preventing coalescence.

Table 1 quantifies these thresholds for different polarity conditions, while Fig. 16 illustrates three representative cases: (a) V* = 0.2 (No coalescence), (b) V* = 0.6 (DC coalescence), and (c) V* = 1.0 ( AC/DC coalescence).

In the DC case (Fig. 16a, V* = 0.2), the displacement threshold is very low (E_disp = 0.25 kV/mm) compared with the corresponding AC case (0.35 kV/mm). Neither initiation nor completion of coalescence is observed, because once droplets displace under DC they merge directly without a measurable delay. Evaporation is minimal; in fact, lifetime is longest in this regime compared with AC excitation, where evaporation is accelerated. When AC content is introduced (Fig. 16b, V* = 0.6), thresholds increase substantially. For instance, E_disp rises from 0.30 kV/mm (DC) to 0.45 kV/mm (AC). Under DC, coalescence initiates at E_init = 0.43 kV/mm and completes at E_comp = 0.56 kV/mm, while under AC these thresholds are not observed because bridge stability cannot be maintained. This case also exhibits the strongest merging delay, confirming the disruptive role of alternating polarity.

In the predominantly alternating case (Fig. 16c, V* = 1.0), coalescence requires much higher fields. Displacement occurs at 0.39 kV/mm (DC) versus 0.59 kV/mm (AC), while initiation and completion shift from 0.62 and 0.77 kV/mm (DC) to 0.82 and 0.92 kV/mm (AC). In this regime, the evaporation-dominated threshold appears at ~0.8 kV/mm, beyond which evaporation overtakes coalescence. Droplets either fail to merge or undergo rapid disintegration, demonstrating that sustained coalescence cannot be achieved under purely alternating excitation. This contrast arises because DC fields provide a continuous and unidirectional attractive force that steadily drives droplets together, whereas AC fields periodically reverse or weaken the attraction. As a result, any nascent liquid bridge formed under AC forcing is disrupted by the next cycle, requiring higher fields for initiation and preventing stable completion. This effect raises or eliminates observable coalescence thresholds, mimicking the suppression seen under AC excitation. In summary, polarity exerts a decisive influence on droplet interaction regimes. A steady DC drive favors displacement- and coalescence-dominated behavior at relatively low thresholds (e.g., E_disp = 0.39 kV/mm, E_init = 0.62 kV/mm, E_comp = 0.77 kV/mm). Mixed polarity significantly elevates thresholds and produces delayed or incomplete coalescence, while purely alternating polarity enforces an evaporation-dominated regime (E_evap-dom ≈ 0.8 kV/mm), where droplets ultimately vanish rather than merge. Fig. 16 and Table 1 together provide a quantitative framework for these transitions.

## 5. Conclusions

This study presents a systematic numerical comparison of uniform DC and AC electric fields on the behavior of single and paired water droplets. The results show that DC excitation produces continuous and unidirectional electrohydrodynamic forces, resulting in stronger droplet transport and faster evaporation compared to oscillatory AC fields. On average, DC fields shorten evaporation time by ~45 % and more than double the horizontal displacement under comparable conditions. It should be noted, however, that in dual-droplet cases where DC induces early coalescence, the reduced surface-area-to-volume ratio can temporarily prolong evaporation despite ongoing deformation. In contrast, AC fields suppress sustained coalescence, leading to slower but consistently monotonic evaporation trends. In dual-droplet scenarios, DC forcing enables earlier and sustained coalescence, with initiation occurring at E_init = 0.62 kV/mm and completion at E_comp = 0.77 kV/mm (V* = 1). By contrast, AC excitation requires higher fields (E_init = 0.82 kV/mm and E_comp = 0.92 kV/mm) and does not reach completion within the tested range, resulting in intermittent merging events and limited net motion. The principal novelty of this work lies in establishing polarity-dependent threshold values (E_disp, E_init, E_comp, E_evap-dom) that delineate transitions between displacement-, coalescence-, and evaporation-dominated regimes. This mapping provides a first-of-its-kind framework for interpreting polarity effects in electrohydrodynamic droplet systems and supplies benchmark values for experimental validation. These insights also reveal that droplet size influences outcomes: larger droplets exhibit greater displacement and benefit more from electric forcing, while smaller droplets respond best at moderate fields before rapid evaporation dominates. From an application perspective, DC excitation proves most effective for long-range transport, rapid evaporation, and processes such as electrohydrodynamic cleaning, cooling, or microfluidic pumping. Conversely, AC fields may be advantageous where reversible positioning or gentle actuation with minimal evaporation is desirable. The model adopted idealized assumptions (smooth surfaces, uniform internal temperature, negligible capillary fluctuations) to isolate the dominant electrohydrodynamic effects, which may slightly shift absolute values of displacement or evaporation. The two-dimensional formulation also cannot fully capture three-dimensional instabilities, axisymmetric variations, or exact surface-area-to-volume scaling. Furthermore, AC excitation was modeled only as sinusoidal; other waveforms, such as pulsed or square-wave fields, may alter vorticity generation and warrant future study. The framework was benchmarked against experimental results from Li et al. [46], Chen et al. [47], and Huang et al. [48], with deviations below 3 % for evaporation and within 0.09 mm for displacement, confirming predictive accuracy. Future extensions will explore three-dimensional simulations, variable wettability, and the effects of surfactants and thermal gradients, thereby advancing the design of application-oriented electrohydrodynamic systems.

## Nomenclature

D Horizontal diameter (m)
$S_0$ Reference droplet surface area (m)
$R_0$ Reference droplet radius (m)
β Shape factor
θ Slope of evaporation time
Δx Droplet displacement (m)
D_max Maximum droplet displacement (m)
∅ Phase distribution number
φ Phase field function
$u_a$ Air velocity $(\frac{m}{s})$
$v_l$ Water particle velocity $(\frac{m}{s})$
σ Surface tension (N/m)

μ Viscosity (Pa • s)
ρ Density($\frac{Kg}{m^3}$)
$\rho_m$ m sector's density
γ Mobility($\frac{m^2}{V \bullet s}$)
p Pressure Pa
g Gravity ($\frac{N}{m^2}$)
v(t) Applied voltage (V)
$v_0$ Initial voltage (V)
f Frequency (Hz)
$V^*$ Non-dimensional volume (1)
ε Effective permittivity ($\frac{F}{m}$)
$\varepsilon_0$Vacuum permittivity ($\frac{F}{m}$)
$\varepsilon_r$ Relative permittivity ($\frac{F}{m}$)
ϵ Interface thickness (m)
$\epsilon_{in}$ Initial interface thickness
$h_{max}$ Maximum length of mesh
T Maxwell stress tensor ($\frac{N}{m^2}$)
E Electric field ($\frac{V}{m}$)
E_init Coalescence initiation threshold (onset of liquid bridge) ($\frac{V}{m}$)
E_comp Coalescence completion threshold (irreversible merge) ($\frac{V}{m}$)
E_evap –dom Evaporation-Dominated Threshold ($\frac{V}{m}$)

## CRediT authorship contribution statement

**Abdi davoud:** Writing – review & editing, Writing – original draft, Validation, Supervision, Software, Project administration, Methodology, Investigation, Formal analysis, Data curation, Conceptualization. **Bo Li:** Writing – review & editing, Supervision, Software, Resources, Project administration, Funding acquisition, Conceptualization. **Zhen Wu:** Visualization, Software, Methodology, Data curation. **Chuang Wen:** Visualization, Software, Methodology, Investigation. **Chao Wang:** Supervision, Software, Resources, Project administration. **Pouria Farokhi Kojour:** Validation, Software, Methodology. **Davoud Abdi Lanbaran:** Writing – review & editing, Writing – original draft, Validation, Supervision, Software, Project administration, Methodology, Investigation, Formal analysis, Data curation, Conceptualization.

## Declaration of Competing Interest

This work was supported by the National Natural Science Foundation of China (No. 52176203).

## Data availability

Data will be made available on request.

## References

[1] K. Zhang, W. Xiang, J. Liu, Z. Xie, Flexible droplet transportation and coalescence via controllable thermal fields, Anal. Chim. Acta 1277 (2023) 341669.
[2] N. Sahoo, P. Dhar, D. Samanta, Vertical magnetic field aided droplet-impact-magnetohydrodynamics of ferrofluids, Colloids Surf. A Physicochem. Eng. Asp. 633 (2022) 127872.
[3] J. Zhang, K. Peng, Z.K. Xu, Y. Xiong, J. Liu, C. Cai, X. Huang, A comprehensive review on the behavior and evolution of oil droplets during oil/water separation by membranes, Adv. Colloid Interface Sci. (2023) 102971.
[4] B.V. Hokmabad, S. Faraji, T.G. Dizajyekan, B. Sadri, E. Esmaeilzadeh, Electric field-assisted manipulation of liquid jet and emanated droplets, Int. J. Multiph. Flow. 65 (2014) 127–137.
[5] L. Li, C. Zhang, Electro-hydrodynamics of droplet generation in a co-flowing microfluidic device under electric control, Colloids Surf. A Physicochem. Eng. Asp. 586 (2020) 124258.
[6] S. Ren, S. Wang, Z. Dong, J. Chen, L. Li, Dynamic behaviors and self-cleaning property of droplet on superhydrophobic coating in uniform DC electric field, Colloids Surf. A Physicochem. Eng. Asp. 626 (2021) 127056.
[7] Z. Sun, W. Li, Q. Chen, N. Li, S. Weng, Y. Liu, Z. Wang(2023). Effect of electric field intensity on droplet fragmentation in oil-in-water-in-oil (O/W/O) emulsions: A molecular dynamics study. Separation and Purification Technology, 125014..
[8] Y. Liu, M. Andrew, J. Li, J.M. Yeomans, Z. Wang, Symmetry breaking in drop bouncing on curved surfaces, Nat. Commun. 6 (1) (2015) 10034.
[9] A. Kumar, I. Ahmad, M. Pathak, Droplet impact on a hydrophobic surface integrated with electrowetting technique, Colloids Surf. A Physicochem. Eng. Asp. 656 (2023) 130423.
[10] F. Mugele, J.C. Baret, Electrowetting: from basics to applications, J. Phys. Condens. Matter. 17 (28) (2005) 705–774.
[11] P. Dima, P.R. Stubbe, A.C. Mendes, I.S. Chronakis, Electric field charge polarity triggers the organization and promotes the stability of electrosprayed probiotic cells, Food Hydrocoll. 139 (2023) 108549.
[12] D.K. Deka, S. Pati, Electrocoalescence dynamics of two unequal-sized droplets, Colloids Surf. A Physicochem. Eng. Asp. (2023) 131152.
[13] Y. Peng, Z. Liao, Y. Zhang, Y. Fang, Z. Qiu, B. Yu, H. Gong, Analysis of deformation dynamics of droplet in oil under the CPG electric field, Chem. Eng. Res. Des. 183 (2022) 357–367.
[14] C. Yang, Q. Zeng, J. Huang, Z. Guo, Droplet manipulation on superhydrophobic surfaces based on external stimulation: a review, Adv. Colloid Interface Sci. 306 (2022) 102724.
[15] C. Liu, Y. Sun, J. Huanng, Z. Guo, W. Liu, External-field-induced directional droplet transport: a review, Adv. Colloid Interface Sci. 295 (2021) 102502.
[16] W. Du, S. Chaudhuri, A multiphysics model for charged liquid droplet breakup in electric fields, Int. J. Multiph. Flow. 90 (2017) 46–56.
[17] P. Atten, Electrocoalescence of water droplets in an insulating liquid, J. Electrost. 30 (1993) 259–270.
[18] J.S. Eow, M. Ghadiri, Motion, deformation and break-up of aqueous drops in oils under high electric field strengths, Chem. Eng. Process. Process.Intensif. 42 (4) (2003) 259–272.
[19] Q. Sun, D. Wang, Y. Li, J. Zhang, S. Ye, J. Cui, X. Deng, Surface charge printing for programmed droplet transport, Nat. Mater. 18 (9) (2019) 936–941.
[20] B. Li, Z. Wang, V. Vivacqua, M. Ghadiri, J. Wang, W. Zhang, Z. Wang, Drop-interface electrocoalescence mode transition under a direct current electric field, Chem. Eng. Sci. 213 (2020) 115360.
[21] Y. Zhou, B. Li, M. Zhang, Z. Sun, Z. Wang, J. Wang, Effect of dielectrophoresis on the coalescence of binary droplets under a non-uniform electric field, Chem. Eng. Sci. 224 (2020) 115739.
[22] M.R. Behera, A. Dasgupta, S. Chakraborty, Investigation of regimes during partial/complete coalescence of a liquid drop on a liquid pool, Chem. Eng. Sci. 251 (2022) 117460.
[23] F. Mugele, J.C. Baret, Electrowetting: from basics to applications, J. Phys. Condens. Matter. 17 (28) (2005) 705–774.
[24] D.K. Deka, S. Pati, Electrocoalescence dynamics of two unequal-sized droplets, Colloids Surf. A Physicochem. Eng. Asp. (2023) 131152.
[25] J.S. Eow, M. Ghadiri, Drop–drop coalescence in an electric field: the effects of applied electric field and electrode geometry, Colloids Surf. A Physicochem. Eng. Asp. 219 (1-3) (2003) 253–279.
[26] A.T. Yasir, A.H. Hawari, M. Talhami, M. Baune, J. Thöming, F. Du, The impact of electric field on the demulsification efficiency in an electro-coalescence process, J. Electrost. 122 (2023) 103796.
[27] Z. Liu, P. Wang, C. Li, D. Li, Z. Wang, M. Zhang, K. Yu, Combined effect of charges and external electric field on collision-coalescence of microns and nanoscale droplets: a numerical simulation perspective, J. Mol. Liq. 328 (2021) 115376.
[28] D. Yang, H. Sun, M. Li, Q. Li, X. Gao, C. Chen, L. He, Effect of electric field strength and droplet diameter on droplet–interface coalescence mechanism, Chem. Eng. Sci. 282 (2023) 119360.
[29] X. Huang, L. He, X. Luo, K. Xu, Y. Lü, D. Yang, Convergence effect of droplet coalescence under AC and pulsed DC electric fields, Int. J. Multiph. Flow. 143 (2021) 103776.
[30] B. Li, Z. Wang, V. Vivacqua, M. Ghadiri, J. Wang, W. Zhang, Z. Wang, Drop-interface electrocoalescence mode transition under a direct current electric field, Chem. Eng. Sci. 213 (2020) 115360.
[31] W. Liu, Y. Tao, Y. Li, Z. Ge, Q. Wu, Y. Ren, Numerical characterization of transient electrohydrodynamic deformation and coalescence of single-core double emulsion droplets by AC field dielectrophoresis, Chem. Eng. Sci. 277 (2023) 118877.
[32] N. Li, Y. Pang, Z. Sun, W. Li, Y. Sun, X. Sun, H. Zeng, Effects of surfactants on droplet deformation and breakup in water-in-oil emulsions under DC electric field: a molecular dynamics study, Fuel 358 (2024) 130328.
[33] N. Chen, Y. Gan, Y. Shi, Enhanced controllability of droplet evaporation via DC electric field, Chem. Eng. J. 479 (2024) 147488.
[34] D. Li, T. Wang, S. Chen, Q. Liu, Y. Xie, C. Liu, Experimental investigation on the dynamic behavior of small droplet in a uniform DC electric field, J. Electrost. 112 (2021) 103592.
[35] D.A. Lanbaran, P.F. Kojour, C. Wang, C. Wen, Z. Wu, B. Li, Comparative analysis of heat transfer enhancement using direct current and alternating current corona discharge in pin fin arrays, Int. J. Therm. Sci. 214 (2025) 109864.
[36] R. Liu, Y.B. Wang, F.F. Xie, S.W. Yang, H.W. Liu, Y.R. Yang, D.J. Lee, Bouncing dynamics of a nanodroplet impacting a superhydrophobic surface under perpendicular electric fields, Colloids Surf. A Physicochem. Eng. Asp. 630 (2021) 127617.
[37] H. Almohammadi, A. Amirfazli, Droplet impact: viscosity and wettability effects on splashing, J. Colloid Interface Sci. 553 (2019) 22–30.
[38] T. Wacławczyk, On a relation between the volume of fluid, level-set and phase field interface models, Int. J. Multiph. Flow. 97 (2017) 60–77.
[39] W.J. Boettinger, J.A. Warren, C. Beckermann, A. Karma, Phase-field simulation of solidification, Annu. Rev. Mater. Res. 32 (1) (2002) 163–194.
[40] B. Bourdin, G.A. Francfort, J.J. Marigo, Numerical experiments in revisited brittle fracture, J. Mech. Phys. Solids 48 (4) (2000) 797–826.

[41] G.J. Schmitz, B. Böttger, J. Eiken, M. Apel, A. Viardin, A. Carré, G. Laschet, Phase-field based simulation of microstructure evolution in technical alloy grades, Int. J. Adv. Eng. Sci. Appl. Math. 2 (4) (2010) 126–139.
[42] A. Karma, D.A. Kessler, H. Levine, Phase-field model of mode III dynamic fracture, Phys. Rev. Lett. 87 (4) (2001) 045501.
[43] Comsol, A.B. (2015). CFD module user's guide.Multiphysics, C. O. M. S. O. L. (1998). Introduction to comsol multiphysics®. COMSOL Multiphysics, Burlington, MA, accessed Feb, 9, 2018.
[44] J.R. Melcher, Continuum electromechanics, 2, MIT press, Cambridge, 1981.
[45] Y. Tian, H. Wang, Q. Deng, X. Zhu, R. Chen, Y. Ding, Q. Liao, Dynamic behaviors and charge characteristics of droplet in a vertical electric field before bouncing, Exp. Therm. Fluid Sci. 119 (2020) 110213.
[46] B. Li, X. Dou, K. Yu, N. Li, W. Zhang, H. Xu, J. Wang, Molecular dynamics simulations of nanoparticle-laden drop–interface electrocoalescence behaviors under direct and alternating current electric fields, J. Mol. Liq. 344 (2021) 117875.
[47] Y.C. Chen, H.C. Yang, Movement characteristics of the inclined surface flow of the open channel on the nanoscale surface, Heliyon 9 (7) (2023).
[48] L. Huang, L. Chen, P. OuYang, B. Ren, Y. Jia, Investigation of droplet pairs' movement under the electric field generated by matrix electrodes, Chem. Eng. Res. Des. 193 (2023) 420–431.